Rauf, Sajid; Zhu, Bin; Shah, M. A.K.Yousaf; Xia, Chen; Tayyab, Zuhra; Ali, Nasir; Yang, Changping; Mushtaq, Naveed; Asghar, Muhammad Imran; Akram, Fazli; Lund, Peter D.

Tailoring triple charge conduction in $BaCo_{0.2}Fe_{0.1}Ce_{0.2}Tm_{0.1}Zr_{0.3}Y_{0.1}O_{3-\delta}$ semiconductor electrolyte for boosting solid oxide fuel cell performance

Published in:
Renewable Energy

DOI:
10.1016/j.renene.2021.03.031

Published: 01/07/2021

Document Version
Publisher's PDF, also known as Version of record

Renewable Energy 172 (2021) 336–349

Contents lists available at ScienceDirect

Renewable Energy

journal homepage: www.elsevier.com/locate/renene

Tailoring triple charge conduction in $BaCo_{0.2}Fe_{0.1}Ce_{0.2}Tm_{0.1}Zr_{0.3}Y_{0.1}O_{3-\delta}$ semiconductor electrolyte for boosting solid oxide fuel cell performance

Sajid Rauf [a, 1], Bin Zhu [b, *], M.A.K. Yousaf Shah [c, 1], Chen Xia [a], Zuhra Tayyab [a], Nasir Ali [d], Changping Yang [a, g, **], Naveed Mushtaq [b], Muhammad Imran Asghar [a, e, ***], Fazli Akram [f], Peter D. Lund [b, e]

[a] Hubei Collaborative Innovation Center for Advanced Organic Chemical Materials, Faculty of Physics and Electronic Science, Hubei University, Wuhan, Hubei, 430062, China
[b] Jiangsu Provincial Key Laboratory of Solar Energy Science and Technology/Energy Storage Joint Research Center, School of Energy and Environment, Southeast University, No.2 Si Pai Lou, Nanjing, 210096, China
[c] Engineering Research Center of Nano-Geo Materials of Ministry of Education, Department of Materials Science and Chemistry, China University of Geosciences, 388 Lumo Road, Wuhan, 430074, China
[d] Zhejiang Province Key Laboratory of Quantum Technology and Devices and Department of Physics and State Key Laboratory of Silicon Materials, Zhejiang University, Hangzhou, 310027, PR China
[e] New Energy Technologies Group, Department of Applied Physics, Aalto University School of Science, P. O. Box 15100, FI-00076 Aalto, Espoo, Finland
[f] Department of Physics and Energy Harvest-Storage Research Center (EHSRC), University of Ulsan, Ulsan, 44610, Republic of Korea
[g] Faculty of Materials Science and Engineering, Taiyuan University of Science and Technology, Waliu Road 66, Wanboling District, Taiyuan City, Shanxi Province, China

ARTICLE INFO

Article history:
Received 28 November 2020
Received in revised form
18 February 2021
Accepted 7 March 2021
Available online 11 March 2021

Keywords:
Semiconductor
Doping
Triple charge conduction
Energy band alignment
Fuel cell

ABSTRACT

Introducing multiple-ionic transport through a semiconductor-electrolyte is a promising approach to realize the low-temperature operation of SOFCs. Herein, we designed and synthesized a single-phase Ce-doped $BaCo_{0.2}Fe_{0.3-x}Tm_{0.1}Zr_{0.3}Y_{0.1}O_{3-\delta}$ semiconductor-electrolyte possessing triple-charge ($H^+/O^{2-}/e^-$) conduction ability. Two different compositions are synthesized: $BaCo_{0.2}Fe_{0.3-x}Ce_xTm_{0.1}Zr_{0.3}Y_{0.1}O_{3-\delta}$ [x = 0.1–0.2]. The 20% doped Ce composition exhibits an outstanding oxide-ion and protonic conductivity of 0.193 S cm^{-1} and 0.09 S cm^{-1} at 530 °C and the fuel cell utilizing $BaCo_{0.2}Fe_{0.2}Ce_{0.2}Tm_{0.1}Zr_{0.3}Y_{0.1}O_{3-\delta}$ as an electrolyte yields an excellent power density of 873 mW cm^{-2} at 530 °C. Moreover, the fuel cell performed reasonably well (383 mW cm^{-2}) even at a low temperature of 380 °C. Furthermore, the 10% Ce-doped utilized in fuel cell device illustrates lower performance (661 mW cm^{-2} at 530 °C and 260 mW cm^{-2} at 380 °C). Successful doping of Ce supports the formation of oxygen-vacancies at the B-site of perovskite and adjusting the ratio of Fe in the compositions. Moreover, the presence of Tm also assist in the creation of oxygen vacancies. Furthermore, the boosting of electrochemical performance and ionic conductivity of applied materials are enlightened by tuning the energy-band structure via employing the UPS and UV–Vis. The physical characterizations and verification of dual-ions (H^+/O^{2-}) in the semiconductor materials are performed via different electrochemical, spectroscopic, and microscopic techniques. A systematic study revealed triple charge conduction in this promising material, which helps in boosting the electrochemical performance of the LT-SOFC.

* Corresponding author. Jiangsu Provincial Key Laboratory of Solar Energy Science and Technology/Energy Storage Joint Research Center, School of Energy and Environment, Southeast University, No.2 Si Pai Lou, Nanjing, 210096, China.
** Corresponding author. Hubei Collaborative Innovation Center for Advanced Organic Chemical Materials, Faculty of Physics and Electronic Science, Hubei University, Wuhan, Hubei, 430062, China.
*** Corresponding author. New Energy Technologies Group, Department of Applied Physics, Aalto University School of Science, P. O. Box 15100, FI-00076 Aalto, Espoo, Finland.
E-mail addresses: zhu-bin@seu.edu.cn, binzhu@kth.se (B. Zhu), cpyang@hubu.edu.cn (C. Yang), imran.asghar@aalto.fi (M.I. Asghar).
[1] These authors contributed equally.

https://doi.org/10.1016/j.renene.2021.03.031

Nomenclature and abbreviation for regularly used terms

Term/composition

LT-CFCs	Low-temperature ceramics fuel cells
LT-PCFCs	Low-temperature protonic ceramics fuel cells
LT-SOFCs	Low temperature solid oxide fuel cells
$BCFC_{0.1}TZY$	$BaCo_{0.2}Fe_{0.2}Ce_{0.1}Tm_{0.1}Zr_{0.3}Y_{0.1}O_{3-\delta}$
$BCFC_{0.2}TZY$	$BaCo_{0.2}Fe_{0.1}Ce_{0.2}Tm_{0.1}Zr_{0.3}Y_{0.1}O_{3-\delta}$
BZY	Y-doped $BaZrO_{3-\delta}$
SJ	Schottky Junction
SDC	$Sm_{0.2}Ce_{0.8}O_{2-\delta}$
NCAL	$Ni_{0.8}Co_{0.15}Al_{0.05}LiO_2$
UPS	Ultraviolet photoelectron spectroscopy
$BCFC_{0.1}TZY$&$BCFC_{0.2}TZY$	$BaCo_{0.2}Fe_{0.3-x}Ce_xTm_{0.1}Zr_{0.3}Y_{0.1}O_{3-\delta}$ (x = 0.1–0.2)
PVK	Perovskite
20%	Intermediate
10%	Lower

Scripts

H_2	Hydrogen
O^2	Oxide ions
mW cm^{-2}	Milli Watt per square centimeter
Ω cm^2	Ohm. square centimeter
V_b	Valence band
H^+	Proton
M	Molar
(χ^2)	Goodness of factor
S cm^{-1}	Siemen per centimetre
C_b	Conduction band

1. Introduction

Lowering the operating temperature is a developed tendency for the ceramics fuel cells (CFCs) and solid oxide fuel cells (SOFCs) to solve many material and degradation issues that hinder the commercialization of this potential technology. However, at reduced temperatures (<550 °C), SOFC suffers from severe problems including low ionic conduction in the electrolyte resulting in increased ohmic losses and higher charge transfer resistance at the electrodes causing high electrode polarization losses [1]. Instead of the obstacle of ohmic resistance in the electrolyte at low-temperature, there is also a major concern of the fuel cell strongly dependent on the compatibility of components of the cell and the reaction mechanism [2]. SOFC performance and stability have a strong dependency on the compatibility of components of the cell. On the other hand, the conventional SOFCs work at a high temperature above 800 °*C* that impedes the quick-start up and shut-down of operational cycles, degrading the device, and increasing the cost; thus, hindering the commercialization of SOFCs [1]. In traditional SOFCs, O^{2-} ions conducting electrolytes are typically used, such as yttria-stabilized zirconia and doped ceria, which produce H_2O at the chamber; consequently, dilute the fuel gas and decrease the efficiency [3,4]. To overcome all of above discussed bottlenecks, a lot of efforts have been done in the last few decades, e.g., thin-film technology was utilized to decrease the ohmic losses [5,6]. However, challenges still remain, especially the fabrication complexity and expensive instrumentation.

Besides, new kinds of electrolyte membranes (with various conductions) have been introduced to primarily deal with the increased ohmic losses and electrode polarization [5–11]. Various kinds of materials have been reported for electrolyte and cathode application; especially, the perovskite (PVK) materials with different kinds of intrinsic and extrinsic conductivities [12–18]. In the development of PVK oxide materials, Kreuer et al. reported a viable proton conductor, i.e., Y-doped $BaZrO_{3-\delta}$ (BZY), which interestingly constrained the electronic conduction and incorporate a proton (H^+), provided by the fuel (hydrogen-H_2) [19]. The application of proton conducting materials as an electrolyte enables low-temperature (<600 °*C*) operation of the CFCs. Indeed, the enhancement of the ionic transport involving (O^{-2}/H^+) and suppression of electronic conduction is possible due to oxygen vacancies creation [20]. For instance, oxygen vacancies can be created by the incorporation of trivalent cations (Y^{3+}) and substitution of tetravalent cations (Zr^{4+}). Owing to the low activation energy for protons to transport, thus, an adjustment of the vacancies enabled rapid transport of the available protons. Other possible mechanisms for the creation of protonic defects include the dissociative adsorption of water from the environment, assisting the generation of more hydroxyl groups (-OH), and supporting proton transportation. In this regard, Mather et al. reported the attractive protonic conduction in LaNbO material. They have well explained the formation of oxygen vacancies and the creation of defects through appropriate doping to achieve high proton conductivities [21,22]. Irrespective of the creation and transport of oxygen vacancies and low-temperature operation, pure protonic materials encountered the issue of chemical instability in the CO_2 and H_2O atmosphere. Therefore, proton-conducting perovskite oxides failed to compete with the conventional electrolytes and still lag behind the intermediate temperature SOFC; thus, alternative materials are needed [23].

Moreover, significant progress has been made in the oxide materials maintaining pure protons, dual ions, and triple charge conductions, respectively. For instance, Ding et al. developed dual-ions (H^+/O^{2-}) an electrolytes membrane $BaZr_{0.1}Ce_{0.7}Y_{0.1}Yb_{0.1}O_{3-\delta}$ (BZCYYb) utilized in SOFCs, which yielded peak power densities of 452 mW cm^{-2} at 700 °*C* [24]. Furthermore, a triple charge ($H^+/O^{-2}/e^-$) conducting BCFZY ($BaCo_{0.4}Fe_{0.4}Zr_{0.1}Y_{0.1}O_{3-\delta}$) PVK oxide materials have been reported as a cathode by heavily Co and Fe doping at the B-site of BZY and achieved power density of 445 mW cm^{-2} at 500 °*C* and many others are reported previously [14,25–27]. It should be noted that heavily doped BZY (with transition metals) has still maintained the ionic conduction. The attractive characteristics of triple charge conducting materials can enable the fuel cell operation even at a low operating temperature of 350 °*C*. Besides, Rauf et al. developed a triple charge conducting semiconductor $Ba_{0.5}Sr_{0.5}Co_{0.1}Fe_{0.7}Zr_{0.1}Y_{0.1}O_{3-\delta}$, where $Ba_{0.5}Sr_{0.5}Co_{0.1}Fe_{0.7}Zr_{0.1}Y_{0.1}O_{3-\delta}$-$Ca_{0.04}Ce_{0.80}Sm_{0.16}O_{2-\delta}$ and $Ba_{0.5}Sr_{0.5}Co_{0.1}Fe_{0.7}Zr_{0.1}Y_{0.1}O_{3-\delta}$ exhibited good electrolytic and cathodic properties, respectively [7]. The prepared cathode materials achieved an excellent fuel cell performance via formation of heterostructure with SCDC at 520 °*C* and the possible operation was performed till 370 °*C*. Recently, Xia et al. has successfully designed a p-n semiconductor heterostructure $BaCo_{0.4}Fe_{0.4}Zr_{0.1}Y_{0.1}O_{3-\delta}$-ZnO as the electrolyte and proposed a heterojunction concept to suppress the electronic conduction while

enabling high ionic conductivity at 550 °C [28]. Subsequently, our group has reported an interesting triple charge conducting layered-structure transition-metal oxide Mg-doped $LiCoO_2$ (LMCO) and tuned their ionic conductivity by forming a heterostructure with an ionic conductor (SDC) for advanced SOFCs. The energy band alignment has induced high ionic conduction via engineered interface semiconductor heterostructure with an outstanding ionic conductivity (0.35 S cm^{-1}) along with remarkable fuel cell performance of 0.7 W cm^{-2} at 600 °C [29]. Therefore, new semiconducting materials with dual ions and triple charge conduction are favorable for fuel cells to realize superior ionic conductivity and high electrochemical performance at low operating temperature. The functional semiconductor electrolyte membranes have been characterized in LT-ceramics fuel cells (LT-CFCs) and LT-SOFCs with variety of conduction properties, such as the co-existence of dual hybrid conduction (O^{2-}/H^{+}) and triple charge ($O^{2-}/H^{+}/e^{-}$) conduction mechanism but not interpreted precisely, which need more attention.

In this work, we fabricated a doped $BaCo_{0.2}Fe_{0.3-x}Ce_xTm_{0.1}Zr_{0.3}Y_{0.1}O_{3-\delta}$ (x = 0.1–0.2) semiconducting electrolyte with triple charge conduction, where the 20% Ce doped BCFTZY modulated the appropriate triple charge conduction for the better fuel cell performance of 873 mW cm^{-2} with high ionic conduction 0.193 S cm^{-1} and stable OCV of 1.09 V at 530 °C comparatively. We also employed 10% Ce-doped $BaCo_{0.2}Fe_{0.2}Ce_{0.1}Tm_{0.1}Zr_{0.3}Y_{0.1}O_{3-\delta}$ ($BCFCe_{0.1}TZY$) as a cathode, where BZY and $Sm_{0.2}Ce_{0.8}O_{2-\delta}$ (SDC) were utilized as electrolyte membranes. The $BCFCe_{0.1}TZY$ demonstrated valid cathodic property. Moreover, the appropriate doping concentration of Ce and the presence of Tm support in the creation of high content of oxygen vacancies where a large number of oxygen vacancies enabled the fast-ionic transport. The protonic charge conduction was also verified via the accomplished method using the O^{2-}/e^{-} filtration layer of BZY. All these accumulated and combined properties in semiconducting materials will pave the way towards a well-functioning electrolyte for the LT-SOFCs.

2. Experimental work

2.1. Materials synthesis and characterizations

The hydrothermal technique assisted by co-precipitation was employed to synthesis various compositions of $BaCo_{0.2}Fe_{0.3-x}Ce_xTm_{0.1}Zr_{0.3}Y_{0.1}O_{3-\delta}$ (x = 0.1–0.2). Barium nitrate ($Ba(NO_3)_2$), Iron nitrate hexa-hydrate ($Fe(NO_3)_3\cdot 6H_2O$), Zirconium nitrate ($Zr(NO_3)_4$), Cobalt nitrate hexa-hydrate ($Co(NO_3)_2\cdot 6H_2O$), and Yttrium nitrate hexa-hydrate ($Y(NO_3)_3\cdot 6H_2O$) obtained from Sigma Aldrich (99.99%), Thulium nitrate hexa-hydrate ($Tm(NO_3)_3.6H_2O$), Cerium nitrate hexa-hydrate ($Ce(NO_3)_3.6H_20$) and Sodium carbonate (Na_2CO_3) from MACKLIN (99.99%) were used as precursors in the synthesis of desired materials without any further purification. The weighed quantity of $Ba(NO_3)_2$, $Fe(NO_3)_3\cdot 6H_2O$, $Co(NO_3)_2\cdot 6H_2O$, $Y(NO_3)_3\cdot 6H_2O$, $Tm(NO_3)_3.6H_2O$, and $Zr(NO_3)_4$ were dissolved in de-ionized water (DI) step-wise under continuous stirring to obtain the 1.0 M homogenous solution. Afterward, the calculated quantity of 20% of $Ce(NO_3)_3.6H_20$ (MACKLIN -99.99%), were added according to the doping ratio into the above solution with continuous stirring. In parallel, another 1.0 M solution of sodium carbonate Na_2CO_3 was prepared as a precipitating agent under stirring continuously. Furthermore, the precipitating agent solution was added dropwise into the above solution to prepare dark brownish precipitates and stirred them for a certain time to get homogenously precipitates solution. The solution was then shifted into an autoclave bottle and put in the vacuum furnace at 180 °C for 6 h, afterward, the autoclave was removed from the vacuum furnace and cool down to room temperature. The obtained precipitates were filtered and washed several times with DI-water and absolute ethanol and then followed by drying at 120 °C for 6 h in the oven. The dried dark brownish powder was ground and sintered at 1100 °C for 6 h with a ramp of 3 °C min^{-1} and then well-ground in agate mortal to obtain the homogenous powder of $BaCo_{0.2}Fe_{0.1}Ce_{0.2}Tm_{0.1}Zr_{0.3}Y_{0.1}O_{3-\delta}$ ($BCFCe_{0.2}TZY$). The powder was further used for physical and electrochemical characterizations. Similarly, the 10% doping ratio of Ce such as $BaCo_{0.2}Fe_{0.2}Ce_{0.1}Tm_{0.1}Zr_{0.3}Y_{0.1}O_{3-\delta}$ powder was prepared for further process.

The crystallographic analysis and the doping effect of Ce (x = 0.1–0.2) into BCFTZY were studied via an X-ray diffractometer (XRD) assisted by the Bruker D8 advanced X-ray diffractometer (Germany, Bruker Corporation). The crystal structure was analyzed using the ProfSuit software [30,31]. The surface morphology of the designed materials and the cross-section of the fuel cell device was studied via the Field emission scanning electron microscope (FE-SEM, JEOL JSM7100F field, Germany). The high resolution-transmission electron microscopy (HR-TEM, JEOL JEM-2100F) operating under an accelerating voltage of 200 kV was employed to study the micro-structure of the prepared materials. The energy band gaps of two prepared materials with different ratios of dopants were obtained via UV–Vis absorption spectra using a UV3600 spectrometer (MIOSTECHPTY Ltd.). Moreover, the ultraviolet photoelectron spectroscopy (UPS) was employed to deduce the valence band level under the unfiltered He–I (21.22 eV) gas discharge lamp and a total instrumental energy resolution of 100 meV, respectively. Besides, the chemical states and surface charge transfer of designed materials were studied via x-ray photoelectron spectroscopy using Al Kα radiation (1486.7 eV). CASA XPS software was used to analyse the XPS results.

2.2. Fuel cell device fabrication

There are three components involve in the fabrication of fuel cell device, anode, cathode, and electrolyte. Initially, electrodes were prepared by mixing the weighed quantity of $Ni_{0.8}Co_{0.15}Al_{0.05}LiO_2$ powder (NCAL powder commercially obtained from the Tianjin Bamo Company (TBC)) into the appropriate volume of terpineol mixing media to obtain a slurry, which was subsequently painted on circular shaped Ni-foam before experiencing desiccation at the 120 °C for 0.45 h to form well dried NCAL pasted Ni-foam (NCAL-Ni) electrodes. The single and symmetrical fuel cell device was fabricated by compacting the homogenous powder of $BCFCe_{0.2}TZY$ between the two NCAL-Ni electrodes uniaxially at the load of 250 MPa to construct a single pellet. The architecture of the designed cell is Ni-NCAL/$BCFCe_{0.2}TZY$/NCAL-Ni of approximate thickness 1.5 mm and an active area of 0.64 cm^2. The silver paste was applied on both sides of the cell to apply as a current collector. Similarly, the other single-cell for $BCFCe_{0.1}TZY$ was also fabricated in the same way. Subsequently, all the fuel cells were online sintered before electrochemical characterizations at 600 °C for 0.45 h to thermally activate the cell.

Besides, the verification of protonic conductivity of $BCFCe_{0.2}TZY$ was investigated by constructing cell of $BCFCe_{0.2}TZY$ between two O^{2-}/e^{-} filtration layers of BZY to only allow the protonic ions transfer with the structure of BZY/$BCFCe_{0.2}TZY$/BZY and then assemble the fuel cell device in the same procedure as described above [32]. The tri-layers of the electrolyte was sandwiched between two pieces of NCAL-Ni electrodes to form the configuration five-layers of Ni-NCAL/BZY/$BCFCe_{0.2}TZY$/BZY/NCAL-Ni. The thickness and the active area are the same as for the general fuel cell device. Moreover, the fuel cell performance has a strong link with the catalytic activity of the electrode; therefore, we investigated the oxygen reduction reaction (ORR) activity of the $BCFCe_{0.1}TZY$. The possible oxygen reduction reaction (ORR) of the triple charge conducting materials was also demonstrated by following this

architecture for two different cells Ni–BCFCe$_{0.1}$TZY/SDC/NCAL-Ni and Ni–BCFCe$_{0.1}$TZY/BZY/NCAL-Ni, where BCFCe$_{0.1}$TZY was applied as a cathode and NCAL-Ni as an anode. However, all the working conditions, prior to and during the electrochemical performance of fuel cell remain the same at every stage of experiments.

2.3. Electrochemical characterizations

The electrochemical performance of fuel cell was measured using an electronic load IT8511 (ITECH Electrical Co., Ltd., China) equipped with a control and data recording software IT7000, with a scan speed of 0.02 A s^{-1} in the current-voltage sweep under the temperature range of 530-380 °C. The dry hydrogen and air were used as fuel and oxidants at the flow rate (120–150 mL min^{-1}), respectively. Moreover, the electrochemical impedance spectroscopy (EIS) measurement was executed via the Gamry Reference 3000 electrochemical workstation (Gamry Instruments, USA) to study the electrical properties and the impedance losses at various components of the design fuel cells. The frequency range for EIS was 0.1–10^5 Hz with an applied AC-voltage with an amplitude of 10 mV in open-circuit voltage (OCV) condition. ZSimpwin software was used for fitting and analyzing the measured data using an appropriate equivalent circuit model.

3. Result and discussion

3.1. Phase and surface morphology analyses

XRD patterns of the optimally sintered BCFCe$_{0.1}$TZY and BCFCe$_{0.2}$TZY materials with 2θ = 15° –80° are presented in Fig. 1 (a, b). All compositions show only one phase with typical pseudo-cubic PVK diffraction peaks. Within the resolution limits of XRD, no secondary phases or impurities can be detected, confirming that the starting reagents completely reacted to form the homogenous compounds with the pure pseudo-cubic crystal structure during sintering. In Fig. 1 (b), a distinct peak shift is shown by a dotted reference line and highlighted. Examination of this pattern illustrates that there is a slight variation in the position and intensities of the reflections for the observed compositions. The peaks shift to a lower diffraction angle with increasing Ce content up to 20%, indicate a lattice expansion. This lattice expansion mainly occurred due to a difference in the ionic radii and charge mismatch of the A/B-site cations. Such a variation will be further discussed in the refinement result of the crystal structure.

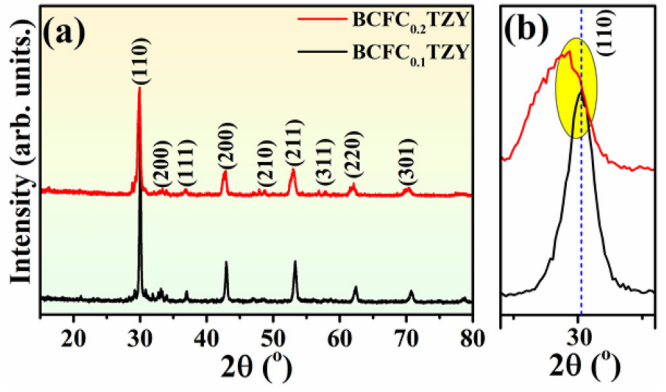

Fig. 1. XRD-patterns of (a) BaCo$_{0.2}$Fe$_{0.3-x}$Ce$_x$Tm$_{0.1}$Zr$_{0.3}$Y$_{0.1}$O$_{3-\delta}$ (x = 0.1–0.2) in the angle (2θ) ranges 15°–80°; (b) an enlarged view of the XRD patterns with a noticeable peak shift straight dotted line.

Fig. 2(a and b) show Rietveld refinement of the XRD patterns for pristine BCFCe$_{0.1}$TZY and BCFCe$_{0.2}$TZY semiconducting materials. The calculated patterns are shown by solid red curves, and the black empty bullet shows the observed intensities, while the differences between the observed and calculated intensities are presented by solid blue curves with a violet bar space group. Apparently, the diffraction peaks of the as-prepared target (shown in Fig. 2(a and b)) can be indexed as a typical layered pseudo-cubic structure with space group Pm3m. A single-phase of pseudo-cubic crystal structure was obtained for all the specimens yielding excellent goodness of factor ($\chi^2 \leq 2.58$). The crystal lattice parameters and unit cell volume for both the compositions were determined from the crystal structure refinement, as shown in Table 1. The average crystallite size and micro-strain were calculated using Williamson-Hell (W–H) analysis based on the refinement raw data files [33].

The morphology and particle size change as a result of the increased concentration of Ce doping in BaCo$_{0.2}$Fe$_{0.3-x}$Ce$_x$Tm$_{0.1}$Zr$_{0.3}$Y$_{0.1}$O$_{3-\delta}$ (where x = 0.1, and 0.2) are studied by FE-SEM, as shown in Fig. 2(c and d). The increase of doping changes the morphology of the particles. The images depict that particles are agglomerated and tend to shrink more towards the nano-size. It can be observed that the particle size of both lower and intermediate doped Ce is in the range of 25–30 nm and 15–20 nm, respectively. Besides, the uniform distribution of particles revealed that the particles or grains are well interconnected and compacted [Fig. 2 (d)], such kind of distribution supports the easy transport of charge species. The small grain size supports the fast transport of charge species while the decrease of grain boundaries enables more active sites [34]. Moreover, the FE-SEM images displayed the morphology of the Ni-foam utilized in the fabrication of cell as well at the amplified resolution along with the morphology of pressed Ni-foam shown in the inset, displayed in Fig. S1 (a-b). Besides, the interface of the Ni-mesh with the NCAL particles are extracted through the FE-SEM and the image at amplified resolution shown in Fig. S1 (c-d).

Furthermore, the TEM has been employed to study the microstructure of BaCo$_{0.2}$Fe$_{0.3-x}$Ce$_x$Tm$_{0.1}$Zr$_{0.3}$Y$_{0.1}$O$_{3-\delta}$ (x = 0.1–0.2). The two images investigated by TEM of BCFCe$_{0.1}$TZY and BCFC$_{0.2}$TZY at the amplification of 100 nm presented in supporting data [Fig. S2(a-b)], where the particles are agglomerated and their size is decreased significantly with the increase of Ce doping concentration, which are analogous and projected in the SEM images displayed in Fig. 2(c and d). Further, high-resolution TEM (HR-TEM) has been employed to study line spacing of the Ce doped BaCo$_{0.2}$Fe$_{0.3-x}$Ce$_x$Tm$_{0.1}$Zr$_{0.3}$Y$_{0.1}$O$_{3-\delta}$ (where x = 0.1, and 0.2). The two images of d-spacing are provided, where well-defined crystalline fringes are formed with lattice spacings of 0.27 nm and 0.265 nm corresponds to the (110) plane of BCFCe$_{0.1}$TZY and BCFCe$_{0.2}$TZY as shown in Fig. 2(e and f).

Moreover, High energy diffraction spectroscopy (EDS) was employed to study the line scanning and elemental mapping to demonstrate the proof of various doping ratios visually, shown in Fig. 3. The line scanning was conducted for specific elements to show their dominant presence and various doping ratios of Ce and adjustment of Fe at B-site in designed materials at the selected specific area as an illustrative line scan shown in the inset of Fig. 3(a). However, with an increase of Ce doping a decrease in Fe content occurred proved via line scan curves, indicating that doping was achieved successfully (Fig. 3(a)). The overall elemental distribution of Ba, Co, Fe, Ce, Tm, Zr, and O was determined by considering the high-angle annular dark-field (HAADF) area of 200 nm is shown in Fig. 3(b). Moreover, the respective mapped image and their corresponding elements in the compositions are displayed in Fig. 3(c–j), respectively.

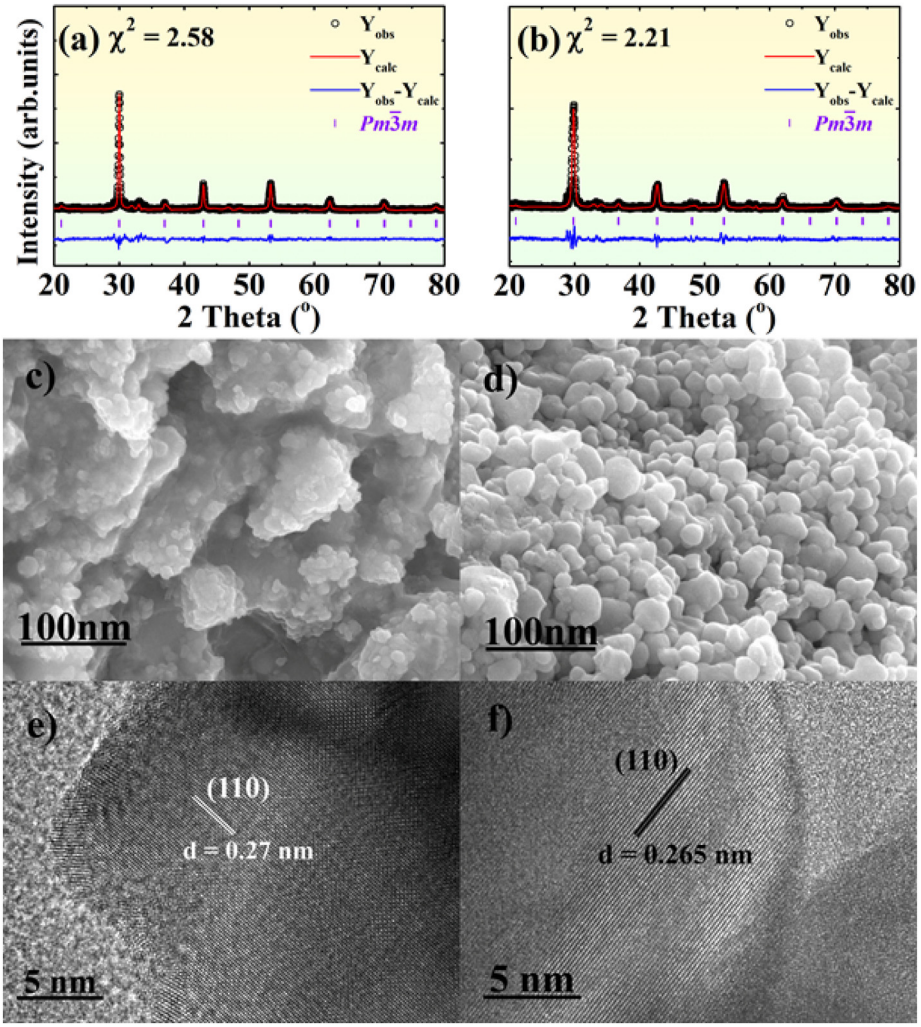

Fig. 2. (a–b) Rietveld refinement via FullProf Suite of XRD spectra; (c–d) Surface morphology study via FE-SEM view at same 100 nm scale; (e–f) Two typical HR-TEM images of the both doped materials showing the d-spacing of as-prepared $BaCo_{0.2}Fe_{0.3-x}Ce_xTm_{0.1}Zr_{0.3}Y_{0.1}O_{3-\delta}$ (x = 0.1–0.2).

Table 1
The detailed crystal structure parameters were carried out by Rietveld refinement via FullProf Suite.

Samples	Space Group	Lattice constants ($a = b = c$) (Å)	Lattice volume (Å^3)	Lattice Angles ($\alpha = \beta = \gamma$)	Average crystallite size (Å)	Micro strain	R_{wp}	R_{exp}	χ^2
0.1 Ce	$Pm\bar{3}m$	4.21064	74.652	90°	249.0762148	0.0503082	14.70	9.16	2.58
0.2 Ce	$Pm\bar{3}m$	4.23527	75.970	90°	118.7391183	0.00211	13.83	9.29	2.21

3.2. Electrochemical performance

The electrochemical performance of the prepared $BaCo_{0.2}Fe_{0.3-x}Ce_xTm_{0.1}Zr_{0.3}Y_{0.1}O_{3-\delta}$ [x = 0.1–0.2] electrolyte materials was demonstrated to understand the effect of doping. Fig. 4(a and b) shows the I–P and I–V curves of the symmetric fuel cell with a structure of Ni-NCAL/$BCFCe_{0.1}$TZY/NCAL-Ni and Ni-NCAL/$BCFCe_{0.2}$TZY/NCAL-Ni at 380–530 °C under the H_2/air atmosphere. The single cell with $BCFCe_{0.2}$TZY achieved quickly sufficient and higher open-circuit voltages (OCV), i.e., 1.09, 1.08, 1.07, and 1.05 V under the temperature range of 530, 480, 430, and 380 °C with remarkable power densities of 873, 721, 580, and 383 mW cm^{-2}, while the single cell of $BCFCe_{0.1}$TZY has OCV of 1.01–1.03 V and yielded power density of 661, 460, 322, and 260 mW cm^{-2}, respectively. It infers that both types of cells have no leakage of gases; however, the intermediate doping of Ce has displayed higher power output than that of the lower doping concentration of Ce. The intermediate concentration of Ce doping intends to create controlled structural defects, which helped in the generation of appreciable oxygen vacancies as compared to the lower doping concentration as discussed later in XPS analysis. However, the high oxygen vacancies lead to enhance the ionic transport to boost the power density of the designed $BCFCe_{0.2}$TZY electrolyte utilized fuel cell. Besides, the incorporation of 10% Tm^{+3} in the semiconducting materials has been used for two purposes, the creation of oxygen vacancies and boost up the protonic conduction, as previously reported [35,36]. Therefore, the maximum power output (P_{max}) is attributed to the high ionic conductivity (σi) with significant protonic conductivity of the semiconducting electrolyte membrane along with reduced polarization resistance (R_p) and lack of sluggish ORR activity at cathode zone [7,37]. It can be clearly observed that the current densities obtained from the fuel cells are closely

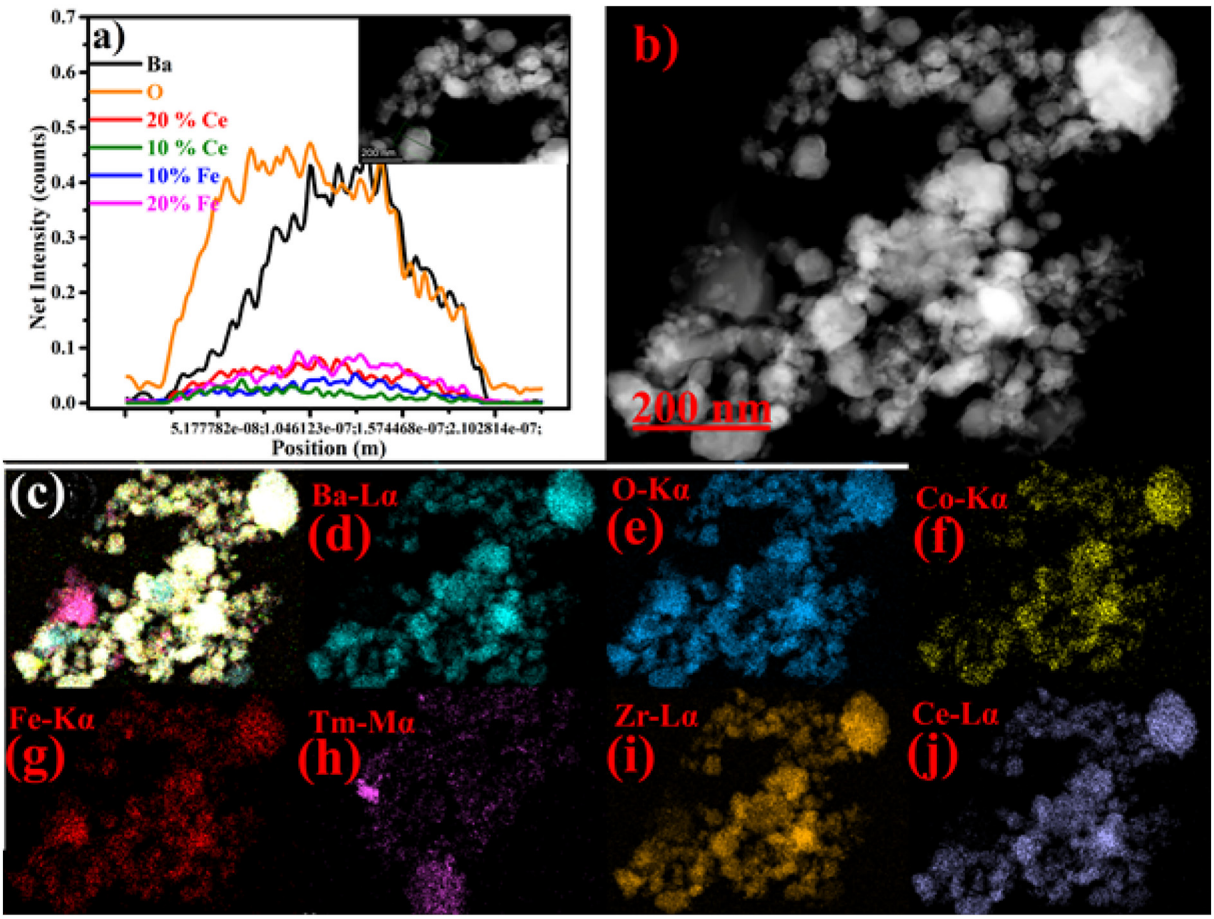

Fig. 3. (a) The line scanning of selected elements via EDS assisted by TEM; (b) HAADF image at 200 nm amplification of selected area; (c–j) the respective EDS mapped selected area and elemental mapping of individual each element of the composite.

associated with the doping ratio of Ce into BCFTZY, as given in Fig. 4(a and b). The OCV, current density, and power output are also dependent on temperature because ionic transport and fuel cell reactions are thermally activated processes, therefore, all these three outcomes partly increased with the increase of temperature. The 20% Ce-doped fuel cells have maintained higher OCV and prevent the issue of short-circuiting as compared to 10% Ce-doped. In this regard, a Schottky junction can be the possible reason for higher OCV and good fuel cell performance, which also played a vital role in stopping the electronic conduction and facilitating the transport of oxide O^{2-} ions towards the anode and will be discussed later.

3.2.1. *Verification of protonic charge species*

Considering the triple charge conduction ($H^{+}/O^{2-}/e^{-}$) reported in BZCFY, BZCeYYbO, and BSCFZY-SCDC, it is anticipated that our designed $BCFCe_{0.2}TZY$ can also present sufficient triple charge conduction as an electrolyte. Thus, to verify the presence of protonic conduction involve in the triple charge conduction, we have employed the BZY layers to block (O^{2-}/e^{-}) and allow only protons to pass through, enabling the determination of proton transport property via electrolyte [32]. The BZY was applied on both sides of the electrolyte $BCFC_{0.2}TZY$ with a fuel cell configuration of Ni-NCAL/BZY/$BCFCe_{0.2}TZY$/BZY/NCAL-Ni. The designed fuel cell delivered power density of 481, 350, and 214 mW cm^{-2} with OCV 1.03, 1.02, and 1.01 V at 530, 480, and 430 °*C*, as shown in Fig. 4(c). The obtained power density has reached half of the total power density of fuel cell with architecture Ni-NCAL/$BCFCe_{0.2}TZY$/NCAL-Ni, however, there is a significant contribution of Tm^{3+} in protonic conduction [36]. The demonstration of OCV more than 1 V illustrates that the electrolyte shows no gas leakage and preventing the short-circuiting risk. This measurement may cause more ohmic losses with limited proton conductivity as a result of additional BZY layers, as well as lowering the OCV of the cell, as observed in Fig. 4(c). Additional contact between BZY and $BCFCe_{0.2}TZY$ also responsible for the polarization loss and can be observed in electrochemical impedance spectroscopy results, which also verifies the proton conduction in the $BCFCe_{0.2}TZY$. It should be noted that the designed materials for proton and oxide ions conduction for the SOFC fueled with H_2 and air. However, the previous report shows that the BZCY related materials or the same structured materials of a mixed ions (proton and oxide) conductor has been reported in SOFC that fueled containing CO contents showed stable operation [15]. Therefore, more likely the prepared semiconductor electrolyte can be employed in fuel cell operated with containing CO fuel. It has been noticed that OCV of various fuel cells with the same electrolyte material has different voltages values at respective temperatures. Therefore, we have tested three different fuel cells to calculate the mean value of OCV based on $BCFCe_{0.2}TZY$ electrolyte membrane at 530–380 °*C* shown in Fig. 4 (d). The calculated mean value of OCV portrays that a very negligible variation occurred at respective temperatures, which inculcate that the designed materials exhibited a stable OCV and promising electrochemical property with some uncertainties in experiments. Usually, there are three

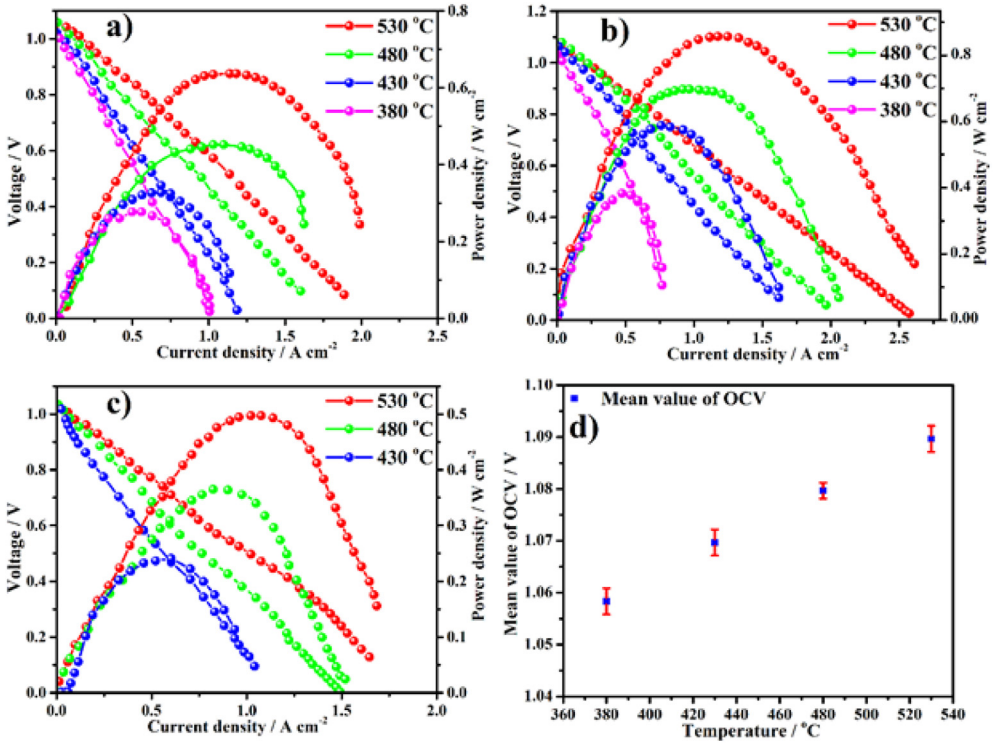

Fig. 4. Electrochemical performance in terms of I–V and I–P curves of stabilized $BaCo_{0.2}Fe_{0.3-x}Ce_xTm_{0.1}Zr_{0.3}Y_{0.1}O_{3-\delta}$ (x = 0.1–0.2) in terms of (a–b) at 530–380 °C ; (c) Protonic fuel cell performance of under the configuration of oxygen blocking layer O^{2-}/e^- of NCAL-Ni/BZY/$BCFCe_{0.2}$TZY/BZY/NCAL-Ni 530–430 °C with H_2 at the anode and airflow at the cathode; (d) Calculated mean value of OCV for three times tested fuel cell with $BCFCe_{0.2}$TZY electrolyte at 530–380 °C.

uncertainties that occurred in experiments. The possibility of uncertainties are like little button cells are used in fuel cell performance measurements, meaning that a small inaccuracy in determining the diameter of the active area could lead to a notable error, for example, with $Ø_{cell}$ = 13 mm and $\Delta Ø_{cell}$ = 1 mm could result in a 17% uncertainty in the area. This affects the reported power density results. Besides, ionic conductivity is calculated based on the resistivity and thickness of the electrolyte layer, meaning that any uncertainty in the thickness value would directly find itself in the ionic conductivity value. For example, if the thickness of the cells is 1–3 mm, then a measurement inaccuracy of 0.2 mm would result in a 10% error in the ionic conductivity. Furthermore, the other possibility of uncertainty in measured data is the reliability and reproducibility of power densities at operational temperature 530 °C, therefore, we verified the reproducibility of results by several times (05) repeated fuel cell measurements that displayed the repeatable and reliable results as shown in Fig. S3. However, the repeated experiments overcome the errors in the presented data.

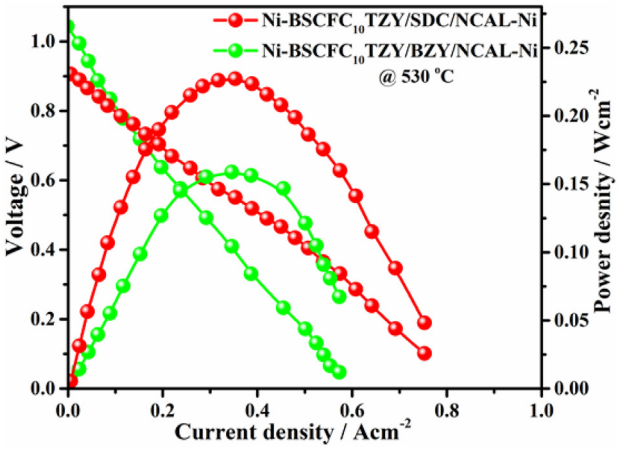

Fig. 5. Electrochemical fuel cell performance of utilizing $BCFCe_{0.1}$TZY as a cathode, BZY, and SDC as electrolyte membrane.

3.3. Oxygen reduction reaction (ORR) catalytic activity

As it is known, cathode plays a crucial role in the ORR process of a fuel cell to create and import oxide ions through the electrolyte to achieve high fuel cell performance and stable OCV for LT-SOFC [14]. Therefore, to prove the concept of triple charge conduction applicability as a cathode, we utilized $BCFCe_{0.1}$TZY semiconductor as a cathode by replacing Ni-NCAL to observe the ORR activity and provided a proof of concept. Thus, two kinds of experiments were performed, such as Ni-NCAL/SDC/$BCFCe_{0.1}$TZY-Ni named as "A" and Ni-NCAL/BZY/$BCFCe_{0.1}$ZY-Ni named as "B". The SDC was used as an oxide ion conductor while the BZY only allow the proton conduction, respectively [19,38]. The below mentioned results shown in Fig. 5 are obtained from these two different steps of two experiments proposed that $BCFCe_{0.1}$TZY maintaining triple charge conduction and successfully utilized as a cathode which showed the capability of $BCFCe_{0.1}$TZY to function as a competent cathode [14,39]. The "A" infers that synthesized $BCFCe_{0.1}$TZY have considerable oxide ions conduction utilizing as a cathode, which generated 232 mW cm^{-2} while the "B" suggested that $BCFCe_{0.1}$TZY has also protonic conduction produced 161 mW cm^{-2}. Such activity has been attributed to ORR in the fuel cell or the functionality of cathode with $BCFCe_{0.1}$TZY that contained the region of electrolyte/electrode. However, utilizing $BCFCe_{0.1}$TZY as a cathode inculcates that the presence of mixed ionic and electronic conduction

facilitates the redox reactions at the electrode/electrolyte interface due to accelerated charge carrier transport, leading to improved catalytic function and also give the confirmation of triple charge conduction. Moreover, the incorporation of SDC as an electrolyte and $BCFCe_{0.1}TZY$ as cathode provided admittance to more active sites for the ORR catalytic activity, which facilitated in the enhancement of the electrochemical performance.

3.4. Electrical characterization of fuel cell device

The detailed electrical properties of the $BaCo_{0.2}Fe_{0.3-x}Ce_xTm_{0.1}Zr_{0.3}Y_{0.1}O_{3-\delta}$ (x = 0.1–0.2) semiconducting materials are studied by EIS measurement in H_2/air, as shown in Fig. 6(a and b). Generally, the EIS can be divided into three portions, where the initial touching point of EIS spectra at the real axis belongs to high frequency, the first semicircle of the EIS curve ascribed to the intermediate frequency region while the large interfacial semicircle intersects at the low-frequency part. All the obtained EIS spectra are simulated by applying a suitable equivalent circuit $LR_0(QR_1)(CR_2)$ through Z-Simpwin software [16]. The simulated data are summarized in Tables (2–3). According to the equivalent circuit, these three parts correspond to the ohmic resistance (R_o) interpret the high-frequency region, charge and mass transfer (R_1 & R_2) of electrolyte and electrodes contribution to EIS spectra corresponds to intermediate and low-frequency regions, respectively.

These parameters are used to correlate them with the dominant charge species available in the fuel cell electrolyte membrane. However, it can be noticed that the R_o and R_p of $BCFCe_{0.2}TZY$ exhibited values of 0.072 Ω cm^2 and 0.328 Ω cm^2 are lower than that of 0.0971 Ω cm^2 and 0.4663 Ω cm^2 in $BCFCe_{0.1}TZY$ enlisted in Tables (2–3). There are several factors responsible for the decrease of R_o and R_p such as, the appropriate concentration of Ce doping,

Table 2
EIS data of $BCFCe_{0.2}TZY$ @ 530, 480, 430 and 380 °C, where R [Ω cm^2], Q [$Y_o[(S\text{-}s)^n$ cm^{-2}]], and C [F-cm^{-2}], where n is frequency power, n [0 < n < 1], respectively. EIS data fitted via ZSIMPWIN software.

Temperature	R_o	R_1	Q_1	L	R_2	C_1	n
$BCFCe_{0.2}TZY$							
530°C	0.072	0.017	0.2238	3.08E-08	0.311	0.6427	0.5206
480°C	0.088	0.024	0.1581	8.69E-08	0.357	0.5611	0.8
430°C	0.1009	0.0542	0.1151	6.31E-08	0.451	0.513	0.42
380°C	0.132	0.0721	0.2716	8.96E-08	0.792	0.314	0.8

Table 3
EIS data of $BCFCe_{0.1}TZY$ @ 530, 480, 430 and 380 °C, where R [Ω cm^2], Q [$Y_o[(S\text{-}s)^n$ cm^{-2}]], and C [F-cm^{-2}], where n is frequency power, n [0 < n < 1], respectively. EIS data fitted via ZSIMPWIN software.

Temperature	R_o	R_1	Q_1	L	R_2	C_1	n
$BCFCe_{0.1}TZY$							
530°C	0.0971	0.0942	0.1792	5.50E-08	0.3721	0.333	0.8
480°C	0.1056	0.1408	0.1348	4.88E-08	0.486	0.2478	0.8
430°C	0.1314	0.1521	0.1245	4.42E-08	0.8102	0.2142	0.4329
380°C	0.1614	0.1874	0.2329	4.00E-08	0.8542	0.1696	0.5444

which produced significant oxygen vacancies, and the presence of Tm^{+3} in the semiconducting materials are responsible for the increase of ionic conduction as previously reported [27,40]. Moreover, junction effect and increase of temperature, all these factors are responsible for the enhancement of ionic conductivity and suppression of electronic conduction. It can be noticed that with the increase of temperature the ohmic resistance and R_1 decrease from 0.132 Ω cm^2 to 0.082 Ω cm^2 and 0.0721 Ω cm^2 to 0.017 Ω cm^2, respectively, due to thermal activation and migration of ions and

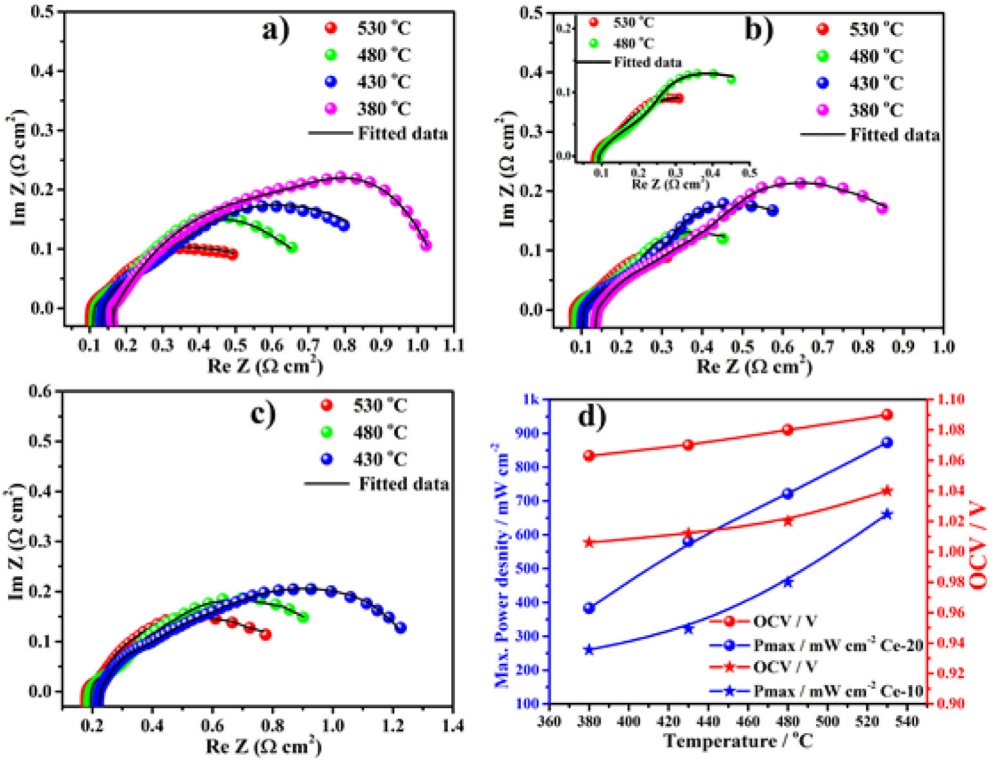

Fig. 6. Electrochemical impedance spectroscopy (EIS) of (a–b) $BaCo_{0.2}Fe_{0.3-x}Ce_xTm_{0.1}Zr_{0.3}Y_{0.1}O_{3-\delta}$ (x = 0.1–0.2) at 530–380 °C; (c) configuration of oxygen blocking layer O^{2-}/e^- of NCAL-Ni/BZY/$BCFCe_{0.2}TZY$/BZY/NCAL-Ni at 530–430 °C with H_2 at the anode and airflow at cathode; (d) comparative study of both doped composition include P_{max} and OCV of $BaCo_{0.2}Fe_{0.3-x}Ce_xTm_{0.1}Zr_{0.3}Y_{0.1}O_{3-\delta}$ (x = 0.1–0.2) at 530–380 °C.

electrons at the grain boundary. In addition, the electrode polarization resistance displays a similar trend that signifies the increase of electrode reaction activity with the increment in temperature 380–530 °C. This also qualifies the high ORR activity at the interface of BCFCe$_{0.2}$TZY/NCAL-Ni. Besides, the BCFCe$_{0.2}$TZY as an electrolyte has provided more active sites for the reaction of the electrode, as a result, promoted the faster catalytic reaction activity and extend the triple-phase boundary (TPB) region due to their triple charge conductivity.

Moreover, the EIS spectra of protonic electrolyte with a five-layer structure Ni-NCAL/BZY/BCFCe$_{0.2}$TZY/BZY/NCAL-Ni were tested, as shown in Fig. 6(c). The EIS spectra were simulated with the same equivalent circuit, however, there are ohmic losses induced by two additional BZY layers and more electrode polarization. The contact interfaces between BZY and BCFCe$_{0.2}$TZY are responsible for the contribution of polarization losses. Therefore, the proposed study of EIS illustration was to illustrate the comparison of pure fuel cell device and the protonic fuel cell device in order to prove the presence of protonic conduction in synthesized BCFCe$_{0.2}$TZY semiconducting electrolyte membrane. Besides, the power densities and OCV are displayed against respective temperatures of both doped compositions as shown in Fig. 6(d). It can be seen that there is an upward trend exhibited in power density and OCV with the increase of Ce-doping at respective temperatures 380, 430, 480, and 530 °C.

In detail, the electrical properties in terms of total and ionic conductivity were obtained from the EIS and I–V curve of the fuel cell device shown in Fig. 7(a and b). The total conductivity is calculated from the EIS spectra involving ohmic resistance include the ionic and electronic resistances and the charge and mass transfer originated with the electrode polarization resistances. It has been reported that ohmic polarization is considered due to ionic resistance of the electrolyte membrane; because NCAL involved as an electrode has high conductivity, therefore, the ohmic resistance is originated from ionic resistances [41].

The ionic conductivity of the Ce-doped BCFTZY electrolyte membrane was estimated from the polarization region of the I–V polarization curve using the ohmic resistance, where the flat part of the I–V curve is considered as an ohmic resistance, also reported previously [28,42–44]. The obtained ionic conductivity of BCFCe$_{0.2}$TZY and BCFCe$_{0.1}$TZY are 0.199–0.08 S cm^{-1} and 0.143–0.044 S cm^{-1} at 530–380 °C, respectively. However, the achieved ionic conductivity is better than that of a previously reported pure ionic conductor; such as SDC~0.05 S cm^{-1} and GDC~0.04 S cm^{-1} at 700 °C, respectively, and ceramic YSZ has 0.13 S cm^{-1} at 1000 °C [45–47]. The prepared materials demonstrated significant protonic fuel cell performance, therefore, the calculated protonic conductivity of BCFCe$_{0.2}$TZY is 0.0902–0.021 S cm^{-1} at 530–430 °C [Fig. 7 (a)]. The attained protonic conductivity is better than that of reported pure protonic materials such as BaCe$_{0.7}$Zr$_{0.1}$Y$_{0.2}$O$_{3-\delta}$ (~0.02 S cm^{-1} at the operating temperature of 700 °C) [48]. Results have proved that high ionic conductivity is the combination of both (O^{2-} and H^{+}) charge species, which is in line with previously reported literature [9].

Herein, we studied the detail of Schottky junction formation as a result of the bi-layer Ni-NCAL/BCFCe$_{0.2}$TZY structure, displayed in Fig. 7(c and d). The rectification phenomenon of the bi-layer Ni-NCAL/BCFCe$_{0.2}$TZY was studied under both H_2/air and air at 530 °C. Initially, the voltage was applied in air and recorded the I–V curve following the Ohm's law, suggesting no formation of a junction in between Cathode (Ni-NCAL) and the layer of BCFCe$_{0.2}$TZY, as shown in Fig. 7(c). Conversely, applying the H_2/Air environment, the reduction process started for 30 min with the supply of H_2, as shown in Fig. 7(d). It was observed that by applying and increase of voltage, simultaneously, the resistance decreased and the current increased, consequently, diode behaviour built and exhibited with time recommend the formation of the Schottky junction between the Ni available at the surface of Ni-NCAL and the semiconductor BCFCe$_{0.2}$TZY [49]. The formation of the Schottky junction is in line with the previous reports [50,51]. The established junction helped in the creation of a built-in electric field (BIEF) in the direction from Ni-metal towards the semiconductor BCFCe$_{0.2}$TZY electrolyte membrane. The intrinsic available electrons in the semiconductor BCFCe$_{0.2}$TZY also help in the enhancement of BIEF, however, in both cases, the BIEF supports the transport of O^{2-} through Ni-metal/electrolyte and impedes the electrons from anode via electrolyte towards cathode to avoid short-circuiting [52]. Schottky junction act as a synergistic junction that overcomes short-circuiting and expedites O^{-2} ions conduction. The SEM cross-sectional view of cell presented in Fig. 7(e and f) of Ni-NCAL/BCFCe$_{0.2}$TZY/NCAL-Ni and O^{-2}/e^{-} blockage layered Ni-NCAL/BZY/BCFCe$_{0.2}$TZY/BZY/Ni-NCAL of fuel cells. The SEM cross-sectional view of both fuel cells displays in Fig. 7(e and f) show that the designed configuration is prepared according to the required architecture cathode/electrolyte/anode for fuel cell technology.

3.5. XPS analysis

XPS was employed to study the chemical state assigned with quantum numbers and the successful formation of single-phase semiconductor BaCo$_{0.2}$Fe$_{0.3-x}$Ce$_x$Tm$_{0.1}$Zr$_{0.3}$Y$_{0.1}$O$_{3-\delta}$ (x = 0.1–0.2). The complete survey of the XPS for both doped compositions are depicting the presence of each constituent element, see Fig. 8(a). High-resolution spectra of Ba, Ce, Fe, and O-1s of Ce doped BCFTZY are displayed in Fig. 8(b–f) while the Co, Tm, Zr, Y, and O-1s spectra are presented in Fig. S4 (a-f). Initially, Ba can be de-convoluted into two main components Ba-3d$_{5/2}$ and Ba-3d$_{3/2}$ at the respective binding energies of 778.6 and 794.8 eV, displayed in Fig. 8(b) and is in line with the previous study [53]. The cobalt element can be de-convoluted into two chemical states Co-2p$_{1/2}$ and Co-2p$_{3/2}$; however, they possess two different oxidation states, i.e., +2 and + 3, respectively. Moreover, the Co-2p$_{3/2}$ with +3 and + 2 oxidation states are assigned at the binding energies of 778.6 eV and 781.0 eV, while the Co-2p$_{1/2}$ with +3 and + 2 oxidation states are assigned at the binding energies of 793.7 eV and 796.3 eV shown in Fig. S4 (a) [54,55]. It can be observed with the 20% Ce doping the Co is tends to reduce from +3 to +2 oxidation states, which infers that there is a creation of oxygen vacancies. Furthermore, it should be noted that the peak height and intensity of Fe decreased with increment of Ce content, as shown in Fig. 8(c). However, there are two spin-orbit Fe-2p$_{3/2}$ and Fe-2p$_{1/2}$ with a satellite peak, where Fe^{2+}-2p$_{3/2}$ and Fe^{2+}-2p$_{1/2}$ corresponds to 709.1 and 722.7 eV and Fe^{3+}-2p$_{3/2}$ and Fe^{3+}-2p$_{1/2}$ corresponds to 710.1 and 724.1 eV and 712.3 and 725.1 eV to Fe^{4+}-2p$_{3/2}$ and Fe^{4+}-2p$_{1/2}$, respectively, while the satellite peak at 717.9 eV [56]. The spin-orbit splitting of Fe-2p (Fig. 8(c)) spectra are well fitted with three valence states, i.e., Fe^{2+}, Fe^{3+}, and Fe^{4+}, respectively. It can be observed that there are different percentages of Fe^{2+}, Fe^{3+}, and Fe^{4+} in both samples, which inculcate that there is a peak shift occurred. Apparently, the average valence state of Fe decreased and a slight shift can be observed from the peak area of each single curve with the increase of Ce doping x = 0.1 and 0.2 [57]. Therefore, the adjustment of B-site cations via the partial substitution of Fe with Ce and the presence of mixed oxidation states of Fe (Fe^{4+}/Fe^{3+} and Fe^{3+}/Fe^{2+}). Consequently, oxygen vacancies are created due to oxidation of the Fe cation (Fe^{2+} to Fe^{3+} and Fe^{3+} to Fe^{4+}) with Ce doping with two different doping concentrations (10% and 20%), as shown in Fig. 8(d and e). The Ce-3d can be de-convoluted into five spin-split doublets, as reported in the literature [58,59]. In Ce-3d, the v (883.3 eV) and u (902.0 eV) peaks correspond to the 3d$_{5/2}$ and 3d$_{3/2}$ contributions derived from

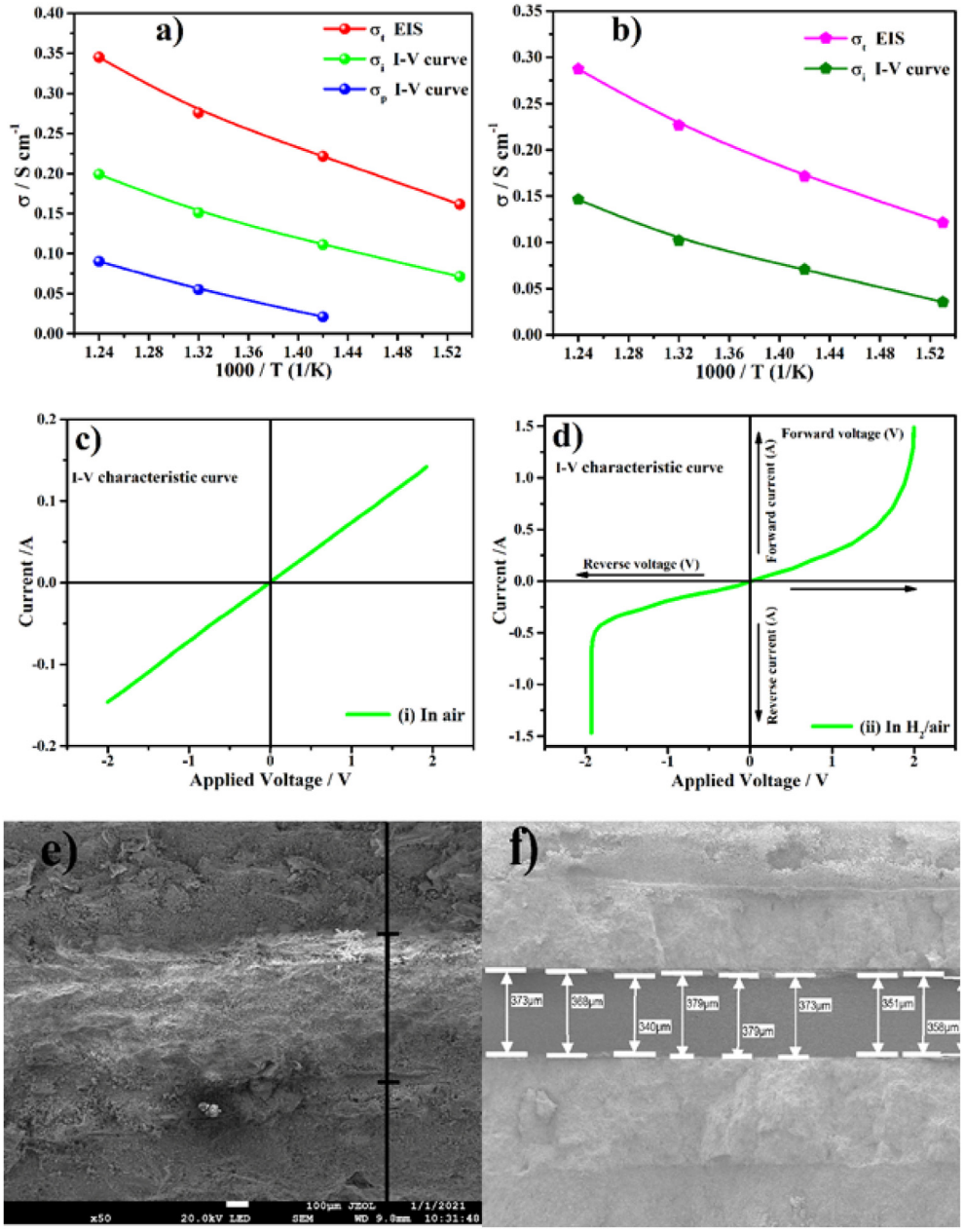

Fig. 7. (a–b)Total conductivity and ionic conductivity of $BaCo_{0.2}Fe_{0.3-x}CexTm_{0.1}Zr_{0.3}Y_{0.1}O_{3-\delta}$ [x = 0.1–0.2] at 530–380 °C and protonic conductivity of under the configuration of oxygen blocking layer O^{2-}/e^{-} of NCAL-Ni/BZY/$BCFCe_{0.2}$TZY/BZY/NCAL-Ni 530–430 °C; (c–d) Rectification curve for the I–V curve under the applied voltage in the Air/H_2 environment at 530 °C; (e–f) SEM fuel cell device cross-section view of the Ni-NCAL/$BCFCe_{0.2}$TZY/Ni-NCAL and NCAL-Ni/BZY/$BCFCe_{0.2}$TZY/BZY/NCAL-Ni.

the spin-orbit coupling as well the cerium ionic states with +3 and + 4 oxidation states. The increase of peak intensity of v_o and u_o indicates the increase of the content of Ce^{+3} on the surface with doping, which can be used as an indicator of the existence of oxygen vacancies. The existence of high content of +3 is linked with more oxygen vacancies [60–62]. The peak heights also became dominant with the increase of Ce doping as shown in Fig. 8 (e). Moreover, the introduction of Tm-4d also helps in the creation of oxygen vacancies, however, the Tm-$4d_{3/2}$ core level with an oxidation state of +3 is assigned at the binding energy of 176.21 ± 0.05 eV accompanied by a small satellite peak observed for $BaCo_{0.2}Fe_{0.2-x}Ce_xTm_{0.1}Zr_{0.3}Y_{0.1}O_{3-\delta}$ (x = 0.1–0.2) shown in Fig. S4 (b) [40]. Furthermore, Fig. S4 (c) illustrates the binding energy peaks at 156 eV and 158.1 eV, conforming to Y-$3d_{5/2}$ and Y-$3d_{3/2}$, respectively [63]. The XPS analysis confirms the position of Zr-3d peaks at 180.6 and 182.9 eV attributed to the Zr-$3d_{5/2}$ and Zr-$3d_{3/2}$, respectively, indicating that Zr-$3d_{5/2}$ and Zr-$3d_{3/2}$ formed the Zr–O bonds. Also, the difference between binding energies is about 2.4 eV, suggesting the existence of Zr^{+4} and Zr^{+3} states, see Fig. S4 (d) [63].

According to the literature, the ionic conduction of any material is intimately concerned with the O-1s BE [64]. Barr and Dong et al. reported that this BE 528–530.5 eV range attributed to the lattice O and highly oxidant O in the oxides materials [65,66]. The O-1s spectra of $BCFCe_{0.2}$TZY and $BCFCe_{0.1}$TZY are displayed in Fig. 8 (f) and Fig. S4 (e–f). The peak at 530.5 eV of $BCFC_{0.1}$TZY represents the lattice oxygen, while the peak of $BCFCe_{0.2}$TZY at 531.8 eV denotes the existence of the –OH ions, which helps to form O-

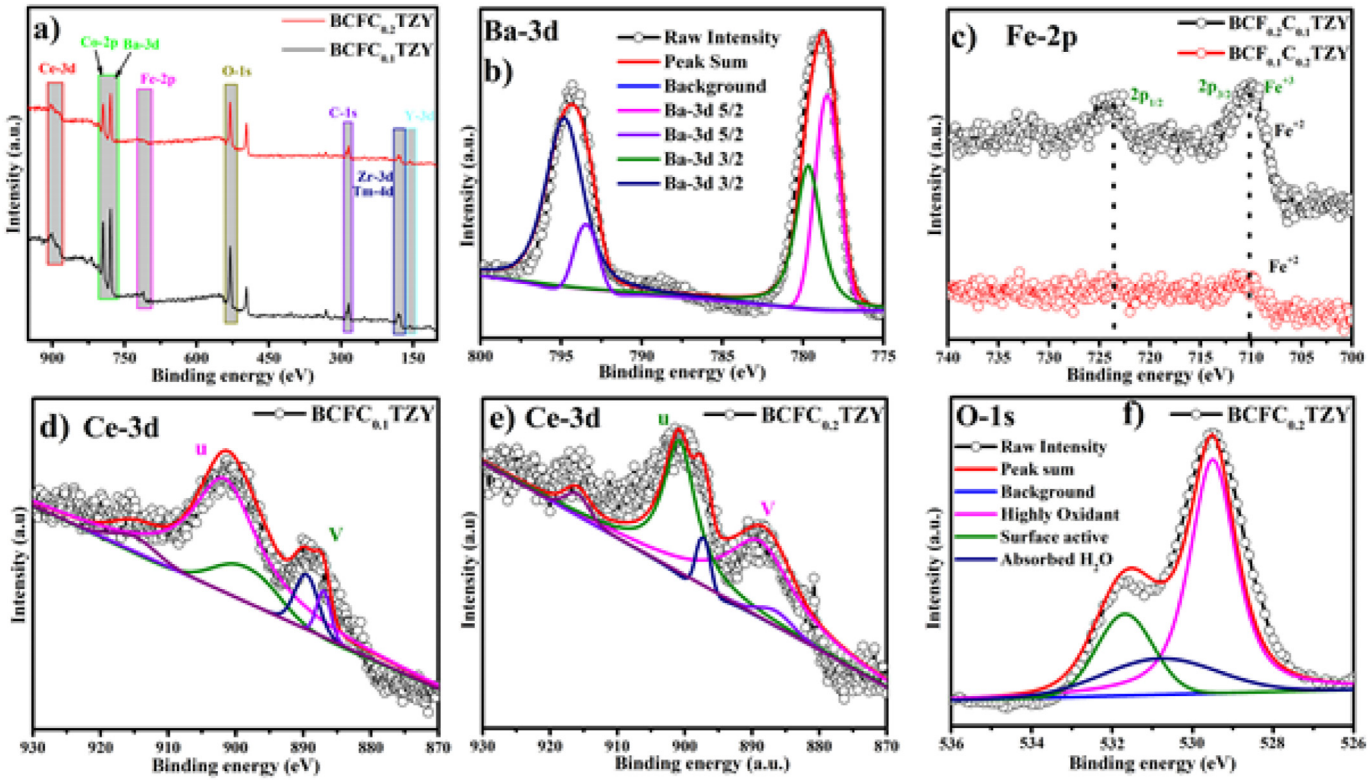

Fig. 8. (a) XPS spectra of $BCFCe_{0.1}TZY$ and $BCFCe_{0.2}TZY$; (b) Ba-3d of $BCFCe_{0.2}TZY$; (c–e) Fe-2p and Ce-3d of $BCFCe_{0.1}TZY$ and $BCFCe_{0.2}TZY$; (f) O-1s spectra of $BCFCe_{0.2}TZY$.

vacancies. It is also observed that increase in doping concentration, the O-1s spectra got broadened towards high binding energy, which directly infers the enhancement of O-vacancies and facilitate the increase in the ionic conductivity of the material, as illustrated in Fig. 8(f) and Fig. S4 (e–f). Thus, broadening of peaks and enlargement of peak area are suggesting that $BCFCe_{0.2}TZY$ has excellent high oxygen vacancies which are capable of fast transport of high ionic conduction.

3.6. UV–Vis and UPS analyses

The arrangement and transport of charge carriers in the semiconductor materials are the important perspective to understand and explain through energy band structure. In this sequence, UV–Vis and UPS were employed to determine the energy band gaps and the valence band maxima to visualize experimental parameters. Initially, UV–Vis was employed to record the absorbance spectra in the range from 350 to 850 nm. There was a sharp peak absorbed and the spectra of $BCFCe_{0.2}TZY$ slightly higher absorbance than $BCFCe_{0.1}TZY$. It can be noticed that there was a redshift occurred at the absorption edge and this redshift signified by attaining the shallow levels in the energy bandgap due to an increase in doping concentration. The optical band gaps of both intermediate and lower concentrations of doping can be calculated via the following relation [67]; $\alpha h\nu = \beta_o(h\nu - E_g)^n$, where α, $h\upsilon$, E_g, β_o, $n = 1/2$ denotes the absorbance coefficient, energy of photons, energy band gap, constant, and the type of bandgap, respectively. The linear part of the graph between $h\upsilon$ and $(\alpha h\upsilon)^2$ meets the x-axis gives the value of bandgap [68]. The obtained energy bandgaps via equation are 2.3 eV and 2.02 eV of $BCFCe_{0.1}TZY$ and $BCFCe_{0.2}TZY$, respectively, which shows that intermediate doping has a lower bandgap value than the 10% Ce-doping as shown in Fig. 9(c and d). These lowering of energy bandgap value suggest the formation of intermediate energy level in between conduction and valence band levels. Additionally, the decrease in the bandgap is also helpful in the reduction of activation energy for the transport of ionic conduction. Therefore, in more detail, the valence band maxima were determined via ultraviolet photoelectron spectroscopy (UPS) having an energy cut-off of 21.2 eV, which is evaluated with He–I photon energy as shown in Fig. 9(a–d). The electrical properties of semiconductors can be controlled by changing the band offset. This implies that the incorporation of impurity atoms in semiconductor oxides can control the Fermi level (EF) associated with modifying the carrier concentration. Therefore, investigation of the valence band offsets is very important to understand changes in the charge carrier concentration, which helps to explain the electrical characteristics. Typical ultraviolet photoelectron spectroscopy (UPS), He (I) spectra are shown in Fig. 9. The valence band maxima are calculated via the following equation [69];

$$\phi = 21.2\ \text{eV} - (E_{cutoff} - E_{onset})$$

Where $h\upsilon$ is the incident He (I) energy at 21.2 eV and where E_{cutoff} is the cutoff energy and E_{onset} is the onset of energy, calculated from UPS. Fig. 9 shows a qualitative energy band diagram based on the energy level parameters calculated from UPS where the calculated Vb values of $BCFCe_{0.1}TZY$ and $BCFCe_{0.2}TZY$ are 5.5 eV and 6.48 eV. Furthermore, the conduction band minima (Cb) were calculated by combination of Vb and the energy bandgap of $BCFCe_{0.1}TZY$ and $BCFCe_{0.2}TZY$ are 3.2 eV and 4.46 eV, respectively. Actually, an increase of oxygen vacancies creates more electron-rich material (basically more n-type) and shrink the energy bandgap. Thus, the Fermi level shifts closer to the conduction band. As a result, the Ce-doped sample's bandgap is subsequently reduced. Additionally, a change in fermi level and EVBM could enhance the density of state (DOS) near the Fermi level, which increases the efficiency of

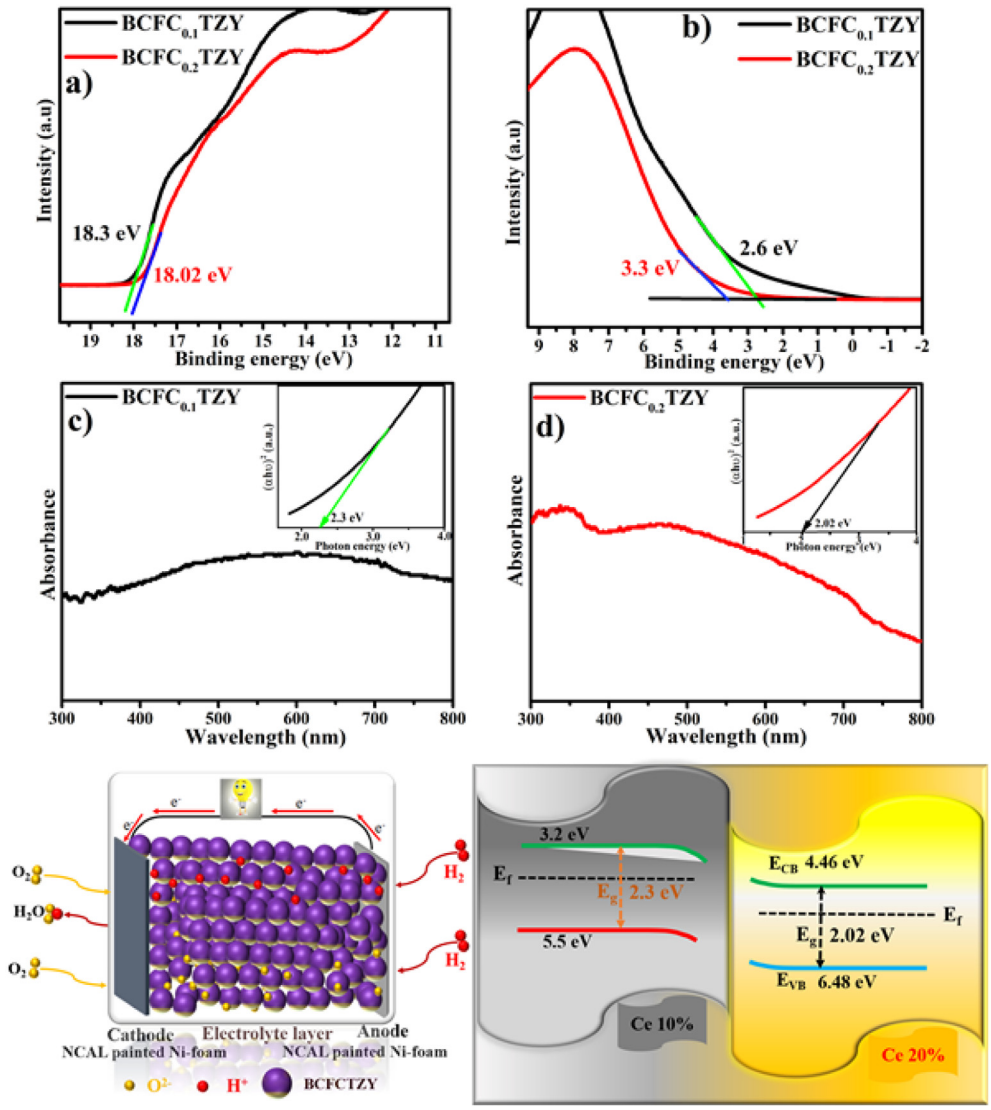

Fig. 9. (a–b) UPS values maintaining E_{cutoff} energy and E_{onset} energy; (c–d) UV–Vis spectra with obtained energy band gaps of $BaCo_{0.2}Fe_{0.3-x}Ce_xTm_{0.1}Zr_{0.3}Y_{0.1}O_{3-\delta}$ [x = 0.1–0.2]; the schematic diagram with energy band alignment structure of $BaCo_{0.2}Fe_{0.3-x}Ce_xTm_{0.1}Zr_{0.3}Y_{0.1}O_{3-\delta}$ [x = 0.1–0.2].

electron transfer to the adsorbed oxygen species O^{2-} and thus reducing the activation energy. This adjustment of bands offset and decrease of energy band gaps provides a smart pathway, which signifying the easy transport of charge carriers and facilitates the fast transport of ions, as a result, enhance the power output of fuel cell.

3.7. Stability of fuel cell

The longer lifetime of the fuel cell in terms of good electrochemical performance and stabilized OCV of semiconducting materials is a prerequisite to commercial use of LT-SOFC. Therefore, a lot of efforts have been put into the long-term and stabilized performance, but the improvement has often been limited [1]. The long-term stability is confronted with various factors such as lab-scale facility of cell fabrication, unavailability of committed technical skills, and effort of a professional engineering enterprise. Using a lab-based facility, we succeeded to accomplish a stable operation of a fuel cell with Ni-NCAL/$BCFCe_{0.2}TZY$/NCAL-Ni yielding 0.87 V stable voltage under a constant current density of 120 mA cm^{-2} for approximately 97 h, see Fig. 10. Indeed, there is a

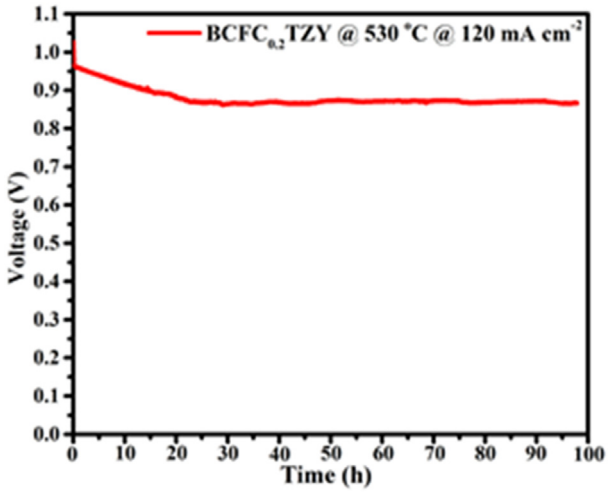

Fig. 10. The durability of $BaCo_{0.2}Fe_{0.1}Ce_{0.2}Tm_{0.1}Zr_{0.3}Y_{0.1}O_{3-\delta}$ as prepared electrolyte under the current density of 120 mA cm^{-2} at 530°C.

great deal of long-term operation required for at least 200 h is mandatory for practical applications but it needs compatible electrodes and good instrumentation.

4. Conclusion

This work presented an effective approach to design and synthesize a novel single-phase perovskite structured electrolyte, $BaCo_{0.2}Fe_{0.3-x}Ce_xTm_{0.1}Zr_{0.3}Y_{0.1}O_{3-\delta}$, which exhibits triple charge conduction. The fuel cell utilizing this promising material as electrolyte produced a high fuel cell performance of 873 mW cm^{-2} with OCV of 1.09 V at 530 °C. Furthermore, a variation in the dopants' composition enables the use of this material as a cathode due to its reasonable ORR activity. We found that an appropriate concentration of Ce doping produces more oxygen deficiencies within the $BaCo_{0.2}Fe_{0.3-x}Ce_xTm_{0.1}Zr_{0.3}Y_{0.1}O_{3-\delta}$ structure and played a key role in enhancing the ionic transport as well as the ORR activity. Both XPS and UPS spectra revealed that Ce doping led to the high oxygen vacancies and shifted the Fermi level closer to the conduction band that ultimately reduced the valence band. Ce-doping can induce appropriate and tailored conduction properties into the semiconductor materials for the LT-SOFC application. Therefore, the obtained results presented not only a solution to solve the hurdles of the electrolytes for LT-SOFCs but also an effective strategy to design effective electrolytes as well as the electrocatalyst perovskite for new advanced LT-SOFCs.

Credit author contribution statement

B.Z., and C.P.Y., conceived the idea, designed the experiments, and analyzed the data. S.R carried out synthesis, characterizations, paper write. MA.K.Y.S., and Z.T., carried out few characterizations and device optimizations. N.A. revised some parts of the manuscript and performed a stability test. S.R., C.X., C.P.Y., B.Z., M.I.A and P.D.L participated in device optimization and data analysis. F.A., analyzed the X.R.D results. S.R., verified fuel cell results. S.R., Z.T., B.Z., and P.D.L. wrote the paper. All authors commented on the manuscript.

CRediT author contribution statement

Sajid Rauf: carried out synthesis, characterizations, paper write, participated in device optimization and data analysis, verified fuel cell results, wrote the paper. All authors commented on the manuscript. **Bin Zhu:** conceived the idea, designed the experiments, and analyzed the data, participated in device optimization and data analysis, wrote the paper. All authors commented on the manuscript. **M.A.K. Yousaf Shah:** carried out few characterizations and device optimizations. **Chen Xia:** participated in device optimization and data analysis. **Zuhra Tayyab:** carried out few characterizations and device optimizations, wrote the paper. All authors commented on the manuscript. **Nasir Ali:** revised some parts of the manuscript and performed a stability test. **Changping Yang:** conceived the idea, designed the experiments, and analyzed the data, participated in device optimization and data analysis. **Naveed Mushtaq:** commented on the manuscript. **Muhammad Imran Asghar:** participated in device optimization and data analysis. **Fazli Akram:** analyzed the X.R.D results. **Peter D. Lund:** participated in device optimization and data analysis, wrote the paper. All authors commented on the manuscript.

Declaration of competing interest

The authors declare that they have no known competing financial interests or personal relationships that could have appeared to influence the work reported in this paper.

Acknowledgement

This work was supported by the National Natural Science Foundation of China (NSFC) under the (grant # 11674085 and 51772080) and National Laboratory of solid-state Microstructures, Nanjing University for project support is also acknowledged. Dr. Asghar thanks the Hubei overseas Talent 100 program (as a distinguished professor at Hubei University) and Academy of Finland (Grant No. 13329016 and 13322738) for their support. Muhammad Akbar helped in the Scanning electron microscope (SEM) images assistance.

Appendix A. Supplementary data

Supplementary data to this article can be found online at https://doi.org/10.1016/j.renene.2021.03.031.

References

[1] L. Fan, B. Zhu, P.-C. Su, C. He, Nanomaterials and technologies for low temperature solid oxide fuel cells: recent advances, challenges and opportunities, Nanomater. Energy 45 (2018) 148–176.
[2] E. Fabbri, L. Bi, D. Pergolesi, E. Traversa, Towards the next generation of solid oxide fuel cells operating below 600° C with chemically stable proton-conducting electrolytes, Adv. Mater. 24 (2) (2012) 195–208.
[3] J. Liu, M. Zhou, Y. Zhang, P. Liu, Z. Liu, Y. Xie, W. Cai, F. Yu, Q. Zhou, X. Wang, Electrochemical oxidation of carbon at high temperature: principles and applications, Energy Fuels 32 (4) (2017) 4107–4117.
[4] O. Yamamoto, Y. Arati, Y. Takeda, N. Imanishi, Y. Mizutani, M. Kawai, Y. Nakamura, Electrical conductivity of stabilized zirconia with ytterbia and scandia, Solid State Ionics 79 (1995) 137–142.
[5] J. Will, A. Mitterdorfer, C. Kleinlogel, D. Perednis, L. Gauckler, Fabrication of thin electrolytes for second-generation solid oxide fuel cells, Solid State Ionics 131 (1–2) (2000) 79–96.
[6] S. de Souza, S.J. Visco, L.C. De Jonghe, Thin-film solid oxide fuel cell with high performance at low-temperature, Solid State Ionics 98 (1–2) (1997) 57–61.
[7] S. Rauf, B. Zhu, M.K.Y. Shah, Z. Tayyab, S. Attique, N. Ali, N. Mushtaq, B. Wang, C. Yang, M.I. Asghar, Application of a triple-conducting heterostructure electrolyte of $Ba_{0.5}Sr_{0.5}Co_{0.1}Fe_{0.7}Zr_{0.1}Y_{0.1}O_{3-\delta}$ and $Ca_{0.04}Ce_{0.80}Sm_{0.16}O_{2-\delta}$ for high performance low-temperature solid oxide fuel cell, ACS Appl. Mater. Interfaces (2020).
[8] L. Malavasi, C.A. Fisher, M.S. Islam, Oxide-ion and proton conducting electrolyte materials for clean energy applications: structural and mechanistic features, Chem. Soc. Rev. 39 (11) (2010) 4370–4387.
[9] C. Zuo, S. Zha, M. Liu, M. Hatano, M. Uchiyama, $Ba(Zr_{0.1}Ce_{0.7}Y_{0.2})O_{3-\delta}$ as an electrolyte for low-temperature solid-oxide fuel cells, Adv. Mater. 18 (24) (2006) 3318–3320.
[10] S. Rauf, B. Zhu, M.Y. Shah, Z. Tayyab, S. Attique, N. Ali, N. Mushtaq, M.I. Asghar, P.D. Lund, C.P. Yang, Low-temperature solid oxide fuel cell based on Tm-doped $SrCeO_{3-\delta}$ semiconductor electrolyte, Mater. Today Energy (2021) 100661, https://doi.org/10.1016/j.mtener.2021.100661.
[11] S. Rauf, M.Y. Shah, B. Zhu, Z. Tayyab, N. Ali, S. Attique, C. Xia, R. Khatoon, C. Yang, M.I. Asghar, Electrochemical properties of a dual-ion semiconductor-ionic $Co_{0.2}Zn_{0.8}O$-$Sm_{0.20}Ce_{0.80}O_{2-\delta}$ composite for a high-performance low-temperature solid oxide fuel cell, ACS Appl. Energy Mater. 4 (1) (2021) 194–207.
[12] A.F. Sammells, R.L. Cook, J.H. White, J.J. Osborne, R.C. MacDuff, Rational selection of advanced solid electrolytes for intermediate temperature fuel cells, Solid State Ionics 52 (1–3) (1992) 111–123.
[13] X. Chen, K. Khor, S. Chan, L. Yu, Influence of microstructure on the ionic conductivity of yttria-stabilized zirconia electrolyte, Mater. Sci. Eng., A 335 (1–2) (2002) 246–252.
[14] C. Duan, J. Tong, M. Shang, S. Nikodemski, M. Sanders, S. Ricote, A. Almansoori, R. O'Hayre, Readily processed protonic ceramic fuel cells with high performance at low temperatures, Science 349 (6254) (2015) 1321–1326.
[15] L. Yang, S. Wang, K. Blinn, M. Liu, Z. Liu, Z. Cheng, M. Liu, Enhanced sulfur and coking tolerance of a mixed ion conductor for SOFCs: $BaZr_{0.1}Ce_{0.7}Y_{0.2-x}Yb_xO_{3-\delta}$, Science 326 (5949) (2009) 126–129.
[16] S. Rauf, M.Y. Shah, N. Ali, N. Mushtaq, Z. Tayyab, M. Yousaf, C.P. Yang, B. Wang, Tuning semiconductor $LaFe_{0.65}Ti_{0.35}O_{3-\delta}$ to fast ionic transport for advanced ceramics fuel cells, Int. J. Hydrogen Energy 46 (15) (2021) 9861–9873.
[17] C. Zhou, J. Sunarso, Y. Song, J. Dai, J. Zhang, B. Gu, W. Zhou, Z. Shao, New reduced-temperature ceramic fuel cells with dual-ion conducting electrolyte and triple-conducting double perovskite cathode, J. Mater. Chem. A 7 (21) (2019) 13265–13274.
[18] R. Lan, S. Tao, Novel proton conductors in the layered oxide material $Li_xAl_{0.5}Co_{0.5}O_2$, Adv. Energy Mater. 4 (7) (2014) 1301683.
[19] K. Kreuer, Aspects of the formation and mobility of protonic charge carriers and the stability of perovskite-type oxides, Solid State Ionics 125 (1–4) (1999) 285–302.

[20] W. Zhou, Z. Shao, Fuel cells: hydrogen induced insulation, Nat. Energy 1 (6) (2016) 16078.
[21] M. Ivanova, S. Ricote, W.A. Meulenberg, R. Haugsrud, M. Ziegner, Effects of A- and B-site (co-) acceptor doping on the structure and proton conductivity of $LaNbO_4$, Solid State Ionics 213 (2012) 45–52.
[22] G.C. Mather, C.A. Fisher, M.S. Islam, Defects, dopants, and protons in $LaNbO_4$, Chem. Mater. 22 (21) (2010) 5912–5917.
[23] E. Fabbri, D. Pergolesi, E. Traversa, Materials challenges toward proton-conducting oxide fuel cells: a critical review, Chem. Soc. Rev. 39 (11) (2010) 4355–4369.
[24] H. Ding, X. Xue, $BaZr_{0.1}Ce_{0.7}Y_{0.1}Yb_{0.1}O_{3-\delta}$ electrolyte-based solid oxide fuel cells with cobalt-free $PrBaFe_2O_{5+\delta}$ layered perovskite cathode, J. Power Sources 195 (20) (2010) 7038–7041.
[25] D. Hashimoto, D. Han, T. Uda, Dependence of lattice constant of Ba, Co-contained perovskite oxides on atmosphere, and measurements of water content, Solid State Ionics 262 (2014) 687–690.
[26] D. Poetzsch, R. Merkle, J. Maier, Proton conductivity in mixed-conducting BSFZ perovskite from thermogravimetric relaxation, Phys. Chem. Chem. Phys. 16 (31) (2014) 16446–16453.
[27] A. Dapčević, D. Poleti, J. Rogan, A. Radojković, M. Radović, G. Branković, A new electrolyte based on Tm3+-doped-Bi2O3-δ type phase with enhanced conductivity, Solid State Ionics 280 (2015) 18–23.
[28] C. Xia, Y. Mi, B. Wang, B. Lin, G. Chen, B. Zhu, Shaping triple-conducting semiconductor $BaCo_{0.4}$ $Fe_{0.4}Zr_{0.1}Y_{0.1}O_{3-\delta}$ into an electrolyte for low-temperature solid oxide fuel cells, Nat. Commun. 10 (1) (2019) 1707.
[29] K.S. Ganesh, B. Wang, J.-S. Kim, B. Zhu, Ionic conducting properties and fuel cell performance developed by band structures, J. Phys. Chem. C 123 (14) (2019) 8569–8577.
[30] J. Rodriguez-Carvajal, FULLPROF a Rietveld and Pattern Matching Analysis Program, Laboratoire Leon Brillouin (CEA–CRNS), Paris France, 2007.
[31] L. McCusker, R. Von Dreele, D. Cox, D. Louër, P. Scardi, Rietveld refinement guidelines, J. Appl. Crystallogr. 32 (1) (1999) 36–50.
[32] Y. Wu, J. Zhang, L. Li, J. Wei, J. Li, X. Yang, C. Yan, C. Zhou, B. Zhu, Proton conduction and fuel cell using the CuFe-oxide mineral composite based on CuFeO2 structure, ACS Appl. Energy Mater. 1 (2) (2018) 580–588.
[33] D. Dorset, X-ray diffraction: a practical approach, Microsc. Microanal. 4 (5) (1998) 513–515.
[34] K. Vikrant, R.E. García, Charged grain boundary transitions in ionic ceramics for energy applications, NPJ Comput. Mater. 5 (1) (2019) 1–12.
[35] M. Laidoudi, I.A. Talib, R. Omar, Study of proton conduction in thulium-doped barium zirconates at high temperatures, J. Phys. Appl. Phys. 33 (23) (2000) 3112.
[36] J.Y. Lin, V. Gupta, S. Cheng, Proton-Conducting Dense Ceramic Membranes for Hydrogen Separation, University of Cincinnati (US), 2004.
[37] M.Y. Shah, N. Mushtaq, S. Rauf, N. Akbar, Y. Xing, Y. Wu, B. Wang, B. Zhu, Advanced fuel cell based on semiconductor perovskite La–$BaZrYO_{3-\delta}$ as an electrolyte material operating at low temperature 550° C, Int. J. Hydrogen Energy 45 (51) (2020) 27501–27509.
[38] M. Liu, D. Ding, Y. Bai, T. He, M. Liu, An efficient SOFC based on samaria-doped ceria (SDC) electrolyte, J. Electrochem. Soc. 159 (6) (2012) B661–B665.
[39] W. He, X. Wu, G. Yang, H. Shi, F. Dong, M. Ni, $BaCo_{0.7}Fe_{0.22}Y_{0.08}O_{3-\delta}$ as an active oxygen reduction electrocatalyst for low-temperature solid oxide fuel cells below 600° C, ACS Energy Lett. 2 (2) (2017) 301–305.
[40] J. Navas, A. Sánchez-Coronilla, T. Aguilar, M. Desireé, N.C. Hernández, R. Alcántara, C. Fernández-Lorenzo, J. Martín-Calleja, Thermo-selective $Tm_xTi_{1-x}O_{2-x/2}$ nanoparticles: from Tm-doped anatase TiO_2 to a rutile/pyrochlore $Tm_2Ti_2O_7$ mixture. An experimental and theoretical study with a photocatalytic application, Nanoscale 6 (21) (2014) 12740–12757.
[41] C. Xia, B. Wang, Y. Ma, Y. Cai, M. Afzal, Y. Liu, Y. He, W. Zhang, W. Dong, J. Li, Industrial-grade rare-earth and perovskite oxide for high-performance electrolyte layer-free fuel cell, J. Power Sources 307 (2016) 270–279.
[42] S. Nho, G. Baek, S. Park, B.R. Lee, M.J. Cha, D.C. Lim, J.H. Seo, S.-H. Oh, M.H. Song, S. Cho, Highly efficient inverted bulk-heterojunction solar cells with a gradiently-doped ZnO layer, Energy Environ. Sci. 9 (1) (2016) 240–246.
[43] B. Zhu, Using a fuel cell to study fluoride-based electrolytes, Electrochem. Commun. 1 (6) (1999) 242–246.
[44] L. Fan, C. Wang, M. Chen, J. Di, J. Zheng, B. Zhu, Potential low-temperature application and hybrid-ionic conducting property of ceria-carbonate composite electrolytes for solid oxide fuel cells, Int. J. Hydrogen Energy 36 (16) (2011) 9987–9993.
[45] Y.P. Fu, S.B. Wen, C.H. Lu, Preparation and characterization of samaria-doped ceria electrolyte materials for solid oxide fuel cells, J. Am. Ceram. Soc. 91 (1) (2008) 127–131.
[46] N. Mahato, A. Banerjee, A. Gupta, S. Omar, K. Balani, Progress in material selection for solid oxide fuel cell technology: a review, Prog. Mater. Sci. 72 (2015) 141–337.
[47] K. Prabhakaran, M. Beigh, J. Lakra, N. Gokhale, S. Sharma, Characteristics of 8 mol% yttria stabilized zirconia powder prepared by spray drying process, J. Mater. Process. Technol. 189 (1–3) (2007) 178–181.
[48] E. Fabbri, A. D'Epifanio, E. Di Bartolomeo, S. Licoccia, E. Traversa, Tailoring the chemical stability of $Ba(Ce_{0.8-x}Zr_x)Y_{0.2}O_{3-\delta}$ protonic conductors for intermediate temperature solid oxide fuel cells (IT-SOFCs), Solid State Ionics 179 (15–16) (2008) 558–564.
[49] Y. Meng, X. Wang, W. Zhang, C. Xia, Y.-n. Liu, M. Yuan, B. Zhu, Y. Ji, Novel high ionic conductivity electrolyte membrane based on semiconductor $La_{0.65}Sr_{0.3}Ce_{0.05}Cr_{0.5}Fe_{0.5}O_{3-\delta}$ for low-temperature solid oxide fuel cells, J. Power Sources 421 (2019) 33–40.
[50] B. Zhu, P.D. Lund, R. Raza, Y. Ma, L. Fan, M. Afzal, J. Patakangas, Y. He, Y. Zhao, W. Tan, Schottky junction effect on high performance fuel cells based on nanocomposite materials, Adv. Energy Mater. 5 (8) (2015) 1401895.
[51] M. Afzal, M. Saleemi, B. Wang, C. Xia, W. Zhang, Y. He, J. Jayasuriya, B. Zhu, Fabrication of novel electrolyte-layer free fuel cell with semi-ionic conductor ($Ba_{0.5}Sr_{0.5}Co_{0.8}Fe_{0.2}O_{3-\delta}$-$Sm_{0.2}Ce_{0.8}O_{1.9}$) and Schottky barrier, J. Power Sources 328 (2016) 136–142.
[52] C. Xia, Z. Qiao, L. Shen, X. Liu, Y. Cai, Y. Xu, J. Qiao, H. Wang, Semiconductor electrolyte for low-operating-temperature solid oxide fuel cell: Li-doped ZnO, Int. J. Hydrogen Energy 43 (28) (2018) 12825–12834.
[53] F. Alema, K. Pokhodnya, Dielectric properties of $BaMg_{1/3}Nb_{2/3}O_3$ doped $Ba_{0.45}Sr_{0.55}Ti_{O3}$ thin films for tunable microwave applications, J Adv. Dielectr. 5 (4) (2015) 1550030.
[54] T. Tsukimori, Y. Shobu, R. Oka, T. Masui, Synthesis and characterisation of $Ba(Zn_{1-x}Co_x)_2Si_2O_7$ ($0 \leq x \leq 0.50$) for blue-violet inorganic pigments, RSC Adv. 8 (16) (2018) 9017–9022.
[55] H. Xia, D. Zhu, Z. Luo, Y. Yu, X. Shi, G. Yuan, J. Xie, Hierarchically structured Co_3O_4@Pt@MnO_2 nanowire arrays for high-performance supercapacitors, Sci. Rep. 3 (1) (2013) 1–8.
[56] T. Yao, C. Guan, J. Zhang, X. Zhang, X. Huang, J. Wu, Preparation of magnetically recyclable yolk/shell FexOy/PdPt@CeO2 nanoreactors with enhanced catalytic activity, Chem Asian J. 12 (12) (2017) 1400–1407.
[57] S. Saher, M. Meffert, H. Störmer, D. Gerthsen, H.J. Bouwmeester, Grain-size dependence of the deterioration of oxygen transport for pure and 3 mol% Zr-doped $Ba_{0.5}Sr_{0.5}Co_{0.8}Fe_{0.2}O_{3-\delta}$ induced by thermal annealing, J. Mater. Chem. A 5 (10) (2017) 4982–4990.
[58] S. Deshpande, S. Patil, S.V. Kuchibhatla, S. Seal, Size dependency variation in lattice parameter and valency states in nanocrystalline cerium oxide, Appl. Phys. Lett. 87 (13) (2005) 133113.
[59] H. Borchert, Y. Borchert, V.V. Kaichev, I.P. Prosvirin, G.M. Alikina, A.I. Lukashevich, V.I. Zaikovskii, E.M. Moroz, E.A. Paukshtis, V.I. Bukhtiyarov, Nanostructured, Gd-doped ceria promoted by Pt or Pd: investigation of the electronic and surface structures and relations to chemical properties, J. Phys. Chem. B 109 (43) (2005) 20077–20086.
[60] B. Liu, Y. Li, S. Qing, K. Wang, J. Xie, Y. Cao, Engineering CuOx-ZrO2-CeO2 nanocatalysts with abundant surface Cu species and oxygen vacancies toward high catalytic performance in CO oxidation and 4-nitrophenol reduction, CrystEngComm 22 (2020) 4005–4013.
[61] M. Piumetti, S. Bensaid, N. Russo, D. Fino, Nanostructured ceria-based catalysts for soot combustion: investigations on the surface sensitivity, Appl. Catal. B Environ. 165 (2015) 742–751.
[62] Q. Shen, M. Wu, H. Wang, C. He, Z. Hao, W. Wei, Y. Sun, Facile synthesis of catalytically active CeO_2 for soot combustion, Catal. Sci. Technol. 5 (3) (2015) 1941–1952.
[63] S. Ji, I. Chang, Y.H. Lee, J. Park, J.Y. Paek, M.H. Lee, S.W. Cha, Fabrication of low-temperature solid oxide fuel cells with a nanothin protective layer by atomic layer deposition, Nanoscale Res. Lett. 8 (1) (2013) 48.
[64] D.A. Pawlak, M. Ito, M. Oku, K. Shimamura, T. Fukuda, Interpretation of XPS O (1s) in mixed oxides proved on mixed perovskite crystals, J. Phys. Chem. B 106 (2) (2002) 504–507.
[65] T.L. Barr, Modern ESCAThe Principles and Practice of X-Ray Photoelectron Spectroscopy, CRC, 1994.
[66] W. Dong, Y. Tong, B. Zhu, H. Xiao, L. Wei, C. Huang, B. Wang, X. Wang, J.-S. Kim, H. Wang, Semiconductor TiO2 thin film as an electrolyte for fuel cells, J. Mater. Chem. A 7 (28) (2019) 16728–16734.
[67] M. Azimi, M. seyed Sadjadi, N. Farhadyar, Fabrication and characterization of core/shell ZnO/gold nanostructures" and study of their structural and optical properties", Orient. J. Chem. 32 (5) (2016) 2517–2523.
[68] S. Singh, Y. Kumar, H. Kumar, S. Vyas, C. Periasamy, P. Chakrabarti, S. Jit, S.-H. Park, A study of hydrothermally grown ZnO nanorod-based metal-semiconductor-metal UV detectors on glass substrates, Nanomater. Nanotechnol. 7 (2017), 1847980417702144.
[69] Z.a. Li, Z. Zhu, C.-C. Chueh, S.B. Jo, J. Luo, S.-H. Jang, A.K.-Y. Jen, Rational design of dipolar chromophore as an efficient dopant-free hole-transporting material for perovskite solar cells, J. Am. Chem. Soc. 138 (36) (2016) 11833–11839.